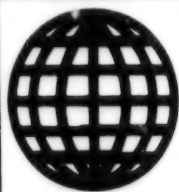


JPRS-JST-93-015

1 APRIL 1993



**FOREIGN  
BROADCAST  
INFORMATION  
SERVICE**

---

# ***JPRS Report***

# **Science & Technology**

---

***Japan***

34TH JSASS/JSME STRUCTURES CONFERENCE

SCIENCE & TECHNOLOGY  
JAPAN

34TH JSASS/JSME STRUCTURES CONFERENCE

936C1015 Tokyo KOZO KYODO NI KANSURU KOENKAI in Japanese 15 Jul 92 pp 1-312

[Selected papers from the 34th JSASS/JSME Structures Conference held 15-17 Jul 92 in Sapporo, Hokkaido, sponsored by the Japan Society for Aeronautical and Space Sciences and the Japan Society of Mechanical Engineers]

CONTENTS

Structural Morphology in Space [Koryo Miura].....	1
Application of Neural Network to Tracking, Rendezvous of Adaptive Structures [Yuji Matsuzaki, Yasuhiro Masunaga, et al.].....	10
Application of Light Aircraft Structure Design To High-Speed Train Body Structure [Kanya Koga, Yoshiharu Noguchi, et al.].....	15
Strength Properties of Oxidation Resistant Three-Dimensional-Fabric/Ceramic Superhigh Temperature Composites [Takashi Ishikawa, Yoichi Hayashi, et al.].....	23
Ultrasonic NDI Results for C/C, CF/Polyimide Composite Components [Masamichi Matsushima, Takashi Ishikawa, et al.].....	30
Heat Structural Analysis for Bent, Double-Sided Radiating Heatpipe Type Radiator for HOPE [Masao Furukawa, Otto Brunner].....	37
Structural Materials for HOPE Reentry Vehicle [Yoshiki Morino, Toshinari Yoshinaka, et al.].....	42

POGO Analysis of H-II Rocket Ground Firing Test [Takumi Ujino, Yujiro Shirai, et al.].....	47
Study on POGO Analysis of Liquid Launch Vehicle [Shigeo Kobayashi, Ken Fukuda].....	53
Tensile Properties of Inconel-718 With Welded Joint [Tomoyuki Hashimoto, Yoshiaki Watanabe, et al.].....	59
Fracture Control of EFFU Graphite Epoxy Strut [Michio Ito, Takane Watanabe, et al.].....	64
Experiment of CFRP Pressurized Composite Tank for Artificial Satellites [Kouichi Miyoshi, Iton Cho, et al.].....	69

## Structural Morphology in Space

936C1015A Tokyo KOZO KYODO NI KANSURU KOENKAI in English 15 Jul 92 pp S2-S10

[Article by Koryo Miura, Institute of Space and Astronautical Science]

### [Text] Introduction

This author has been engaged for many years in the creation of concepts for deployable and related structures for space applications. He found that the really beautiful concepts depend either directly or indirectly on the well-known basic principles of mechanics. It is interesting to note that some of the concepts are directly obtained from minimum/maximum principles of mechanics.

The purpose of this paper is to show how the basic principles of mechanics played an important role when this author conceived and verified some concepts of deployable space structures, which have now become well established. This review may be helpful for researchers and engineers in this field.

### Coilable Longerons and Mastics

Linear deployable structures constitute the basic building block for constructing space structures. They can be used independently, or to construct composite planar and solid structures. Typical mechanisms based on linear deployable structures which can be observed in our daily life are telescopic automobile antennas, carpenter's reels, and foldable scales.

A group of space curves played a key role in the development of space deployable structures which were used successfully for the early space missions such as Voyager. The curves are elastic curves called "Elastica." It is well known that the study of the Elastica was initiated by Euler in his first book on variational calculus. Later, Kirchhoff treated the Elastica in three dimensions. Treaties by Kirchhoff are mentioned in the book "Theory of Elasticity" (Love, 1944).

As shown in Figure 1, a rod can be held so that it has a given twist, and its central-line forms a given helix, by a wrench of force  $K$  and couple  $R$ : the axis of the wrench coincides with the axis of the helix. The force and the



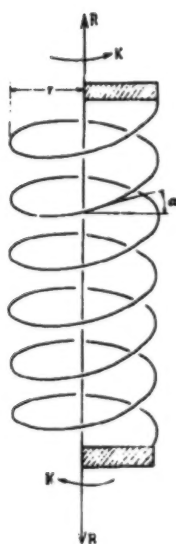


**Figure 1. An Elastic Curve**

couple of the wrench are applied to rigid pieces to which the ends of the rod are attached. The important fact to be noted here is that the helical form can be maintained also by terminal forces alone, without any couple. With reference to deployable structures, this fact indicates the possibility that an elastic rod is stowed in a helical form simply by compressing it by terminal forces applied at the ends of the rod.

A deployable structure using this phenomenon was first realized by the Astro

Research Corporation, and the extendible mast called "Astromast" was successfully deployed in space on board the Voyager spacecraft (Astro, 1978). Excited by the success of the Astromast, the author and his colleagues started a laboratory study of a similar concept. At the time we needed extendable masts for supporting payloads, to be installed in a scientific satellite much smaller than the Voyager spacecraft.

The modified concept, we called it the "Simplex-mast," is shown in Figure 2 (Miura, et al., 1984). The principal components of the Simplex-mast are the coilable continuous longerons (rod), the integrated radial spacers, the diagonal bracing wires, the appropriate hinges, and the traction wire and its motor-driven reel. The three longerons are deformed to helical forms and finally stowed into a coil by the terminal forces applied by the traction wire in the direction of the axis of the mast. Since the elastic large deformation of this composite structure is very complicated, model experiments were necessary to understand the principal characteristics of this structure.

Extensive research and development efforts have been done to apply the concept to a reliable, accurate, and compact extendible mast which meets severe specifications. The 5 m and 3 m long Simplex-masts were fabricated for the magnetometer experiment on board the scientific satellite Akebono. Figure 3 shows a view of the ground testing of the Simplex-mast before launch.

#### Planar Deployable Structures

Large planar structures are mandatory for future space missions. Solar power satellites, space radars, solar sails are some typical examples. These planar structures can be constructed either by deploying a packaged structure or by assembling structural components, which may themselves be deployable.

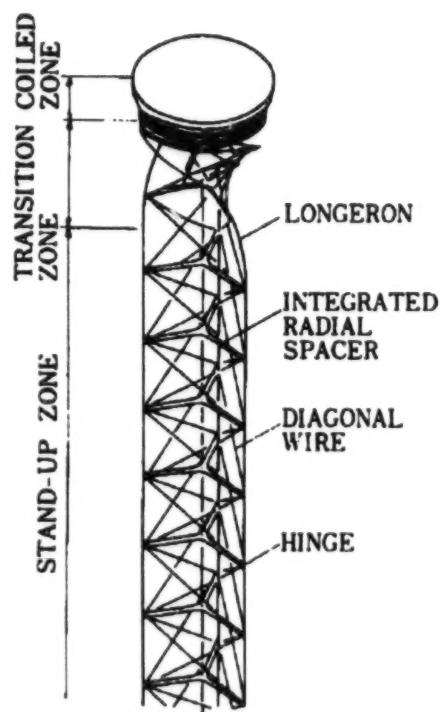


**Figure 2. Simplex-Mast**

In the previous section, we have seen that the *Elastica* studied by Euler and Kirchhoff provided a hint for a rational method of packaging slender elastic bars, and it eventually led to the invention of the Astromast and the Simplex-mast. It is natural to think that, in the case of thin plates, the corresponding *Elastica* may also play a key role in the development of planar deployables.

Depending on loading and boundary conditions, a wide variety of problems belonging to this category can be considered. Among them, the elastic deformation of a thin, infinite plate subjected to bi-axial compression may be a representative problem. This problem can be expressed by the finite deformation differential equation for a thin plate presented by von Karman.

The computation indicates that the bending deformation becomes dominant as the plate thickness decreases. For thin plates, the in-plane strain energy becomes large in comparison with the bending strain energy and hence, according to the principle of locally minimum potential energy, as the wall thickness is decreased, a deformation pattern with smaller in-plane strains and larger bending strains is produced. For an infinitely thin plate, therefore, the deformation should be completely inextensional within the mid-plane of the plate. This result is supported by the computed in-plane strains.

Figure 4 shows 10 solutions, arbitrarily selected from the computed data (Tanizawa and Miura). These deformations feature sharp ridge lines, and are essentially inextensional within the mid-plane. Since the elastic plate problem is parallel to the elastic rod problem, this group of surfaces can be called "elastic surfaces," or "Plate Elastics." It is quite surprising that the elastic surfaces are by no means the smoothly curved surfaces expected by analogy with the rod problems. Because of the property of inextensional deformation, these deformations can be visualized by models made of paper.



Figure 3. Deploying Test of Simplex-Mast on Board Akebono Satellite

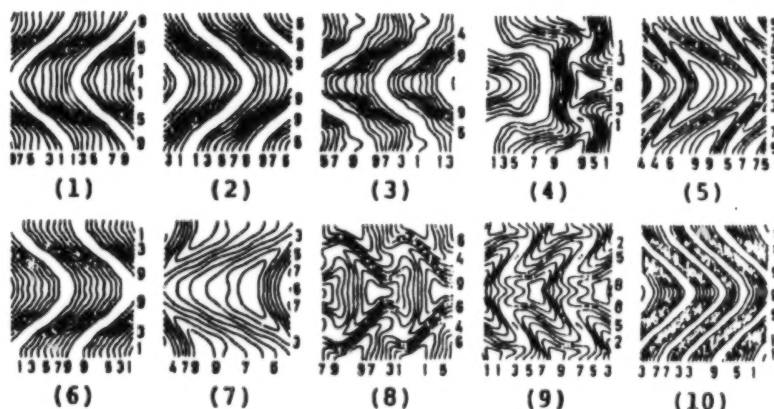


Figure 4. Deformation of Infinite Plate Compressed Bi-Axially (Arbitrary selected 10 solutions, contour map of the fundamental region)

When the least energy solution is sought among these solutions, we obtain the polyhedral surface based on a herringbone-shaped region which is further composed of four congruent parallelograms, as shown in Figure 5. This is exactly the surface presented by the author in relation to Yoshimura's buckling pattern for thin cylindrical shells (Miura, 1970). The surface is developable because the sum of angles around an arbitrary point on the surface is 360 degrees. This surface is named "the developable double corrugation surface (DDC surface)."

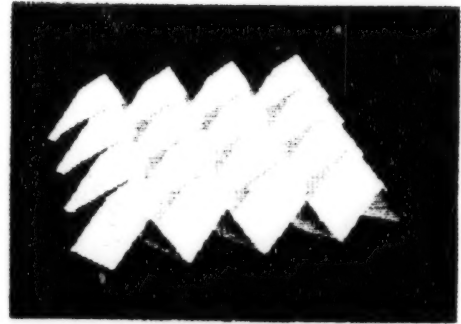


Figure 5. Developable Double Corrugation Surface (DDC surface)

The DDC surface leads to a novel concept for planar deployable structures. By this concept, a plane can be folded in two mutually orthogonal directions at the same time, and in a uniform way. In Figure 8, a series of photographs of a paper model shows how a plane is folded up and contracts simultaneously lengthwise and widthwise. If an ideal paper of vanishing thickness is folded infinitesimally close, then it will fold into a point. This is the transformation of a plane into a point (Miura, 1980, 1985).

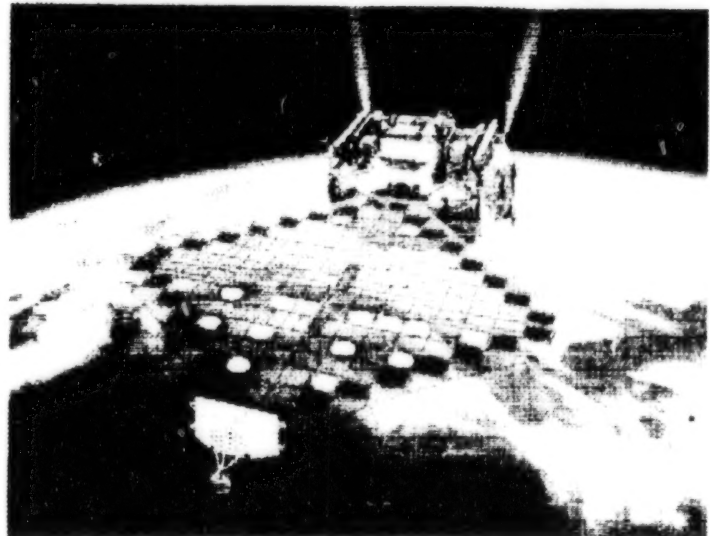


Figure 6. Two-Dimensionally Deployable Array Experiment on Board Space Flyer Unit

Another important characteristic of this deployable structure is that its contraction in the two mutually orthogonal directions are related throughout the folding process. A contraction in the X direction is always accompanied by a contraction in the Y direction, and vice versa.

Now, the plan is under way to launch a two-dimensional deployable array on board the Space Flyer Unit, scheduled for 1995 (Figure 6). The array utilizes the same folding principle described above. It is a thin membrane solar cell array which will be simultaneously deployed in two orthogonal directions, thus, it is called the "two-dimensional deployable array experiment" (Miura and Natori, 1985). This concept of deploying large membranes is also suitable for the sails of solar sail spacecraft.

#### Variable Geometry Truss and Adaptive Structures

For deployable structures, the two extreme configurations, that is, the packed and deployed configurations are important and the intermediate configuration

is usually left out of consideration. After several years of research on deployable structures, this author came to the conclusion that, if a structure can change its configuration step by step and can stay rigid at any step, it has very wide applications. That is, the possibility of structures which can be called variable geometry structures was envisaged. Because the majority of space structures are truss type structures, the variable geometry structure should be sought first in this category. Let it be called a variable geometry truss (VGT).

The concept of the VGT is based on the classical work by A.F. Mobius in 1837. His description of the stability of the truss indicates that, if it is viewed from a new angle, the shape of the truss can be changed. Thus, if the length  $l(ab)$  between the joints a and b is changed, then, the shape of the truss is changed too. Of course, this does not cause any forces in truss members. The original thought of the variable geometry truss concept comes from this reasoning.

It is found that there are only two configurations for the linear statically determinate spatial-truss structure shown in Figure 7. The configuration shown in Figure 7(a) consists of tetrahedral modules, while the configuration in Figure 7(b) consists of octahedral modules. Furthermore, if an equilateral octahedral truss module is used, the truss shown in Figure 8 is obtained. This truss is a symmetry rich structure and is used for the following study.

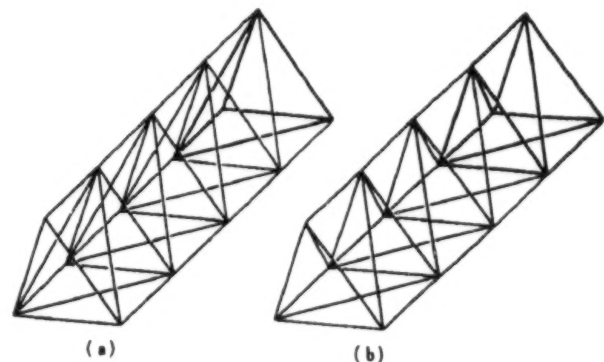


Figure 7. Linear Statically Determinate Spatial Trusses

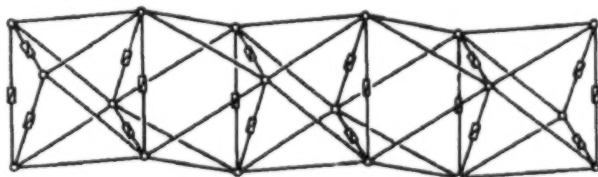


Figure 8. Variable Geometry Truss (VGT)

A variety of VGTs of different characteristics will be obtained depending on the location of the variable length members. The truss, shown in Figure 9, which is equipped with actuators in each lateral member, was originally developed by the ISAS group (Miura, 1984) and NASA group

(Rhodes and Mikulas, 1985) in the middle of the eighties. It has the unique property that the truss is completely collapsed if each lateral member increases its length to three times the original unit length. Conclusively, the VGT can simulate an arbitrary curve in three-dimensional space.

Figure 10 shows three configurations displayed by an eight-module VGT conceptual model (Miura and Furuya, 1985). The length of the diagonal members is 400 mm, and the length of the lateral members can change from 400 mm to 600 mm. Each lateral member is equipped with an actuator and is program controlled by a microcomputer.



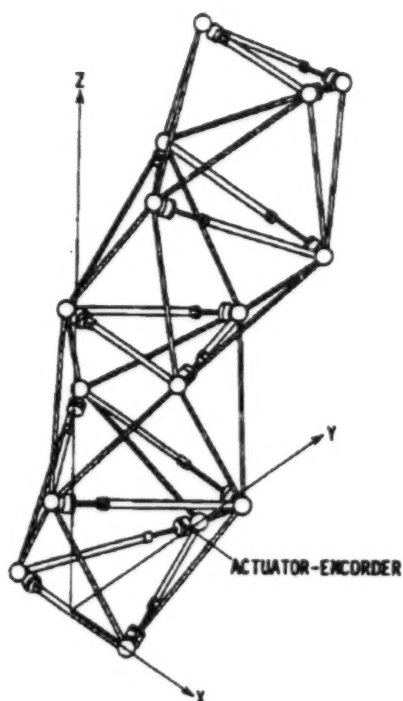


Figure 9. Variable Geometry Truss (VGT)

The theoretical study and demonstration of the VGT concept presented the first clear example for the adaptive structure concept (Miura and Furuya, 1988). Adaptive structures are defined as structural systems whose geometric and inherent structural characteristics can be changed beneficially to meet mission requirements, either through remote commands and/or automatically in response to external stimulations.

#### Tension Truss Antenna

Various structural concepts have been proposed for space-borne large deployable antennas. Among them, antennas constructed by rigid spatial trusses or beams are prevalent. The wrap-rib antenna and the octet-truss antenna are a few examples. As the size of antenna increases, however, larger ones constructed by rigid members will meet serious difficulties caused by increasing weight, packing volume, and number of joints. So, the present author believes that antennas using primarily tensile members will play a major role in future lightweight, large space antennas.

The problem of constructing an antenna reflector surface in three-dimensional space by a latticed tensile structure is, in terms of mathematics, establishing a finite set of lattice points describing, as close by as possible a parabolic surface. For this purpose, this author presented a new concept

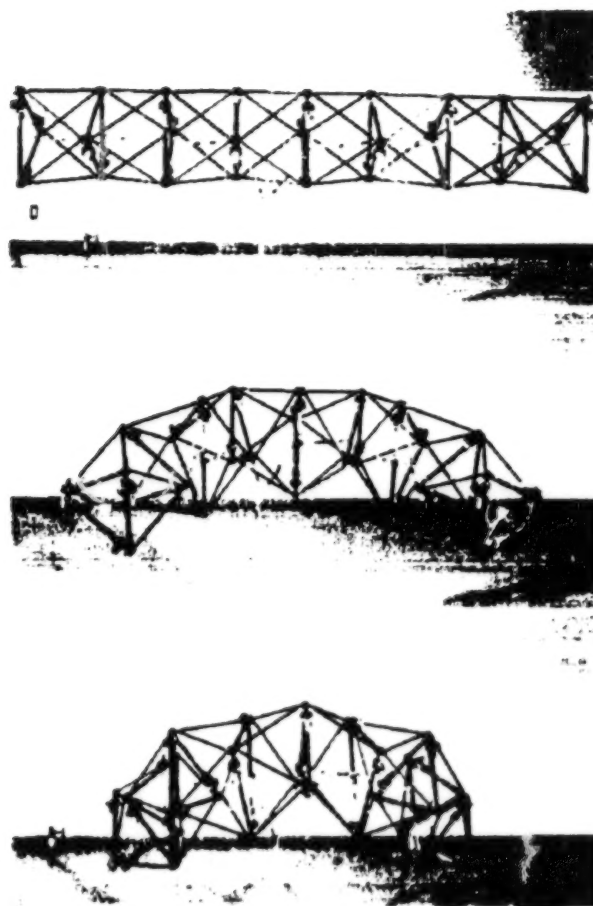


Figure 10. Demonstration by VGT Model

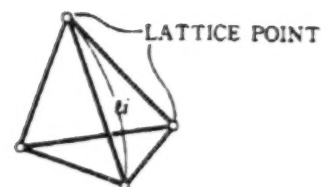
called the tension truss antenna, which is a truss system consisting of tensile members.

Let us consider a tetrahedral truss, as shown in Figure 11. If each member of this truss is replaced by a flexible cable member of identical unstretched length, the cable lattice structure shown in Figure 11(b) is obtained. Then, if an appropriate force is applied to each node of the lattice, so that every cable member is in a state of tension, a three-dimensional rigid structure is formed as shown in Figure 11(c). It is clear that the lattice points determined by the configurations in Figures 11(a) and 11(c) are virtually identical to each other, because the length of corresponding members and their ways of combination are equal. Here, it has been assumed that strains in truss members are negligibly small.

Conclusively, a set of lattice points determined by a truss can be realized by means of a cable lattice structure activated by forces which are exerted by a supporting structure. It should be noted that the shape of the cable lattice structure is primarily determined by geometric quantities only. The forces exerted from supporting structures are used for stretching the cable members, and the effect of stretching on the geometry of the truss is always calculable and is of secondary importance. Thus, the concept of a tension-activated cable lattice structure is established. Since this structure is in essence a truss rather than a lattice structure, it can be called a "tension truss" (Miura and Miyazaki, 1990).

The basic conditions for a tension truss are as follows: each member of the truss is made of a flexible cable and it must be in a state of tension in use, and the truss must be stable and statically determinate.

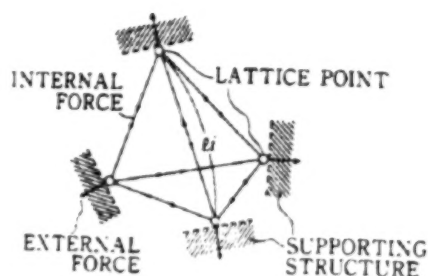
The tension truss concept can be applied to deployable parabolic structures. Figure 12 shows the principles of the tension truss antenna. The most important feature of the tension truss antenna is that its shape is virtually predetermined by geometric quantities such as the length and arrangement of cable members of the truss. External forces are applied only for the purpose of giving the truss tensile forces to reproduce such predetermined shape. The effect of cable stretching on the shape is of secondary importance. Therefore, the concept of tension truss antenna is essentially different from those of current tension structure antennas such as the hoop-column antenna, whose shape is primarily determined by the equilibrium of forces.



(a) RIGID TRUSS



(b) CABLE LATTICE



(c) TENSION TRUSS

Figure 11. Concept of Tension Truss

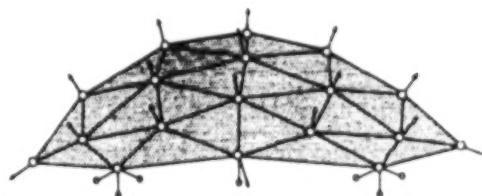


Figure 12. Principles of Tension Truss Antenna

The Space-VLBI program in Japan needs a large, precision antenna more than 10 m in diameter on-board the Muses-B satellite. The antenna is used to receive radio waves from radio stars at 22, 5, and 1.6 GHz bands in a circular polarization. The antenna must be stowed compactly within an envelope of 2,200 mm x 5,200 mm, and the weight should not exceed 220 kg.

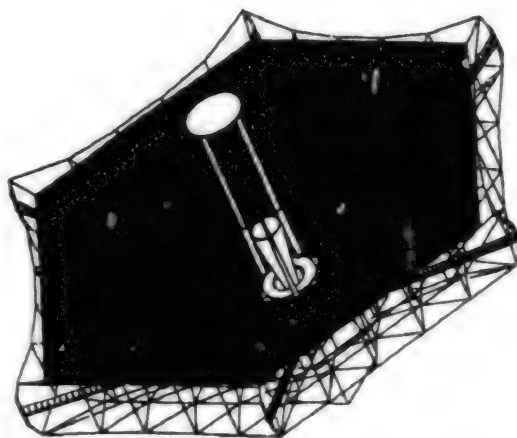


Figure 13. Tension Truss Antenna for VLBI Mission

After feasibility studies on a few proposed concepts, the modified version of the tension truss antenna was selected. As shown in Figure 13, the antenna structure consists of the supporting hub, the feed support column which deploys vertically from the hub, the six extendible columns which deploy radially from the hub, the cable assembly which is tensioned by the above columns, and the reflective metal mesh which is connected to the cable assembly. The cable assembly consists of the tension truss, the secondary cable net which interpolates between the nodes of the tension truss, and the reflecting mesh surface. This assembly is stretched between the terminal ends of radial columns and the central hub. Muses-B satellite will be launched in 1995.

#### Acknowledgements

The author would like to acknowledge Mr. Masamori Sakamaki and Mrs. Yukari Ono for making this work possible.

#### References

1. Astro Research Corp., "Astronauts for Space Applications," 1978, ARC-B-004.
2. Love, A.E.H., "A Treatise on the Mathematical Theory of Elasticity," 4th Ed., Dover Publications, 1944.
3. Miura, K., "Proposition of Pseudo-Cylindrical Concave Polyhedral Shells," Proc. IASS Symposium on Folded Plates and Prismatic Structures," International Association for Shell Structures, Wien, 1970.
4. Ibid., "Method of Packaging and Deployment of Large Members in Space," 31st Congress International Astronautical Federation, Tokyo, 1980, Paper IAF-80 A-31; also, ISAS Report No. 618, Inst. Space Astronautical Science, Japan, 1985.
5. Miura, K., Natori, M., Sakamaki, M., Kakitubo, K., and Yahagi, H., "Simplex-Mast: An Extendible Mast for Space Applications," 14th International Symposium on Space Technology Science, Tokyo, 1984.

6. Miura, K., "Design and Operation of a Deployable Truss Structure," 18th Aerospace Mechanisms Symposium, 1984, NASA CP-2311.
7. Miura, K. and Natori, M., "2D Array Experiment on Board a Space Flyer Unit," SPACE SOLAR POWER REVIEW, Vol 5, 1985.
8. Miura, K. and Furuya, H., "Variable Geometry Truss and Its Application to Deployable Truss and Space Crane Arm," ACTA ASTRONAUTICA, Vol 12 No 7/8, 1985.
9. Ibid., "Adaptive Structure Concept for Future Space Applications," AIAA J., Vol 26 No 8, 1988.
10. Miura, K. and Miyazaki, Y., "Concept of the Tension Truss Antenna," Ibid., Vol 28 No 6, 1990.
11. Rhodes, M.D. and Mikulas Jr., M.M., "Deployable Controllable Geometry Truss Beam," NASA TM 86366, 1985.
12. Tanizawa, K. and Miura, K., "Large Displacement Configuration of Bi-Axially Compressed Infinite Plate," TRANS. JAP. SOC. AERO. SPACE SCIENCES, Vol 20 No 50, 1978.



## **Application of Neural Network to Tracking, Rendezvous of Adaptive Structures**

936C1015B Tokyo KOZO KYODO NI KANSURU KOENKAI in Japanese 15 Jul 92 pp 2-5

[Article by Yuji Matsuzaki, Department of Aerospace Engineering, Nagoya University; Yasuhiro Masunaga, Nomura Research Institute; and Shinji Abe, Graduate Student, Nagoya University]

[Text] **Abstract:** This paper describes a computer simulation analysis on the application of neural network (NN) control to tracking and rendezvous of a moving target. The effectiveness and feasibility of the NN control is thus examined by considering docking example by an adaptive space structure. The simulation example showed that the application of NN control is very effective in the tracking and rendezvous problem.

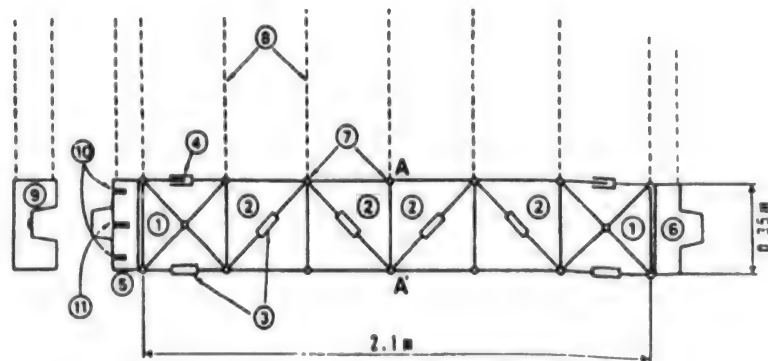
### **1. Introduction**

Since mankind stepped out for the first time into space about the middle of this century, docking of space vehicles in space has taken place many times. At present when various kinds of space projects are in progress, not only the docking of a space station and a spaceplane, but also problems such as maneuvering space floating structures involving gigantic masses whose positioning and attitude control are complex, are becoming important. If conventional methods are to be employed, high-performance computers and observational apparatus are required. However, when there are limitations on the mass and available space of the payload in the space shuttle, etc., it is very desirable to realize these operations using small and light on-board computers. Toward the realization of such objects we have been applying fuzzy control for tracking and rendezvous of docking objects which use space adaptive structures.<sup>1,2,3</sup>

In this research, we have applied a different approach, namely, neural network (NN) to tracking and rendezvous of targets in docking, and investigated its effectiveness. We performed learning of a controller consisting of NN, and simulated the tracking and rendezvous of targets using the controller which has been learned.

## 2. Simulation Model

In this simulation model, a model based on an experimental model (Figure 1<sup>11</sup>) was used. The four modules at the center are shear deformable modules whose length of the diagonal members can be changed by linear actuators, and each module undergoes shear deformation. Bending deformation modules, one on each end, consist of a member on the lower side whose length is controlled by an actuator and a member on the upper side which is elongated and contracted by passive sliding. By means of laser sensors installed on the docking mechanism, the deviation, distance, and inclination of the target can be measured.



- |                                     |   |
|-------------------------------------|---|
| 1. Bending deformation module       | 7. Pin joint                              |
| 2. Shearing deformation module      | 8. Wire                                   |
| 3. Linear actuator                  | 9. Docking target                         |
| 4. Slide mechanism                  | 10. Laser sensor for distance measurement |
| 5. Docking mechanism                | 11. Laser sensor for tracking             |
| 6. Dummy mass for docking mechanism |   |

Figure 1. Plan View of Two-Dimensional Truss Space Adaptive Structure Model

In the simulation model (Figure 2), the positional relationship between the target and the tracking device is considered determinable by the relative distance  $l$  and the relative deviation  $d$  obtained from the data measured by the sensors. In this case,  $d$  is given a positive sign if the target is above the tracking device, and a negative sign if it is below. In this research, we will investigate the tracking and rendezvous of the target by using only actuators 1, 2, and 3 of the shear deformation module.

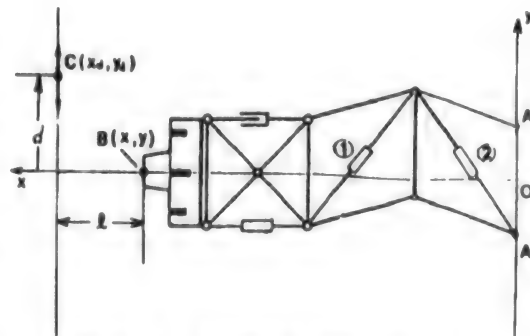


Figure 2. Simulation Model

## 3. Tracking and Rendezvous of Target by Neural Network

### 3.1 Controller Consisting of Neural Network

The controller uses a three-level hierarchical network having an input level (level A), an intermediate level (level B), and an output level (level C). The input consists of the distance  $l$  and the deviation  $d$ , and the output is the elongation or contraction of the actuator. As an example of the input and output relationship of the NN units, if one calls the output of the unit  $u_j^B$  of the intermediate level,  $o_j^B$ , and the coupling weight from the unit  $u_j^B$  to the unit  $u_k^C$ ,  $w_{jk}^B$ , then the sum of the inputs  $i_k^C$  to the unit  $u_k^C$  and the output  $o_k^C$  of the unit  $u_k^C$  are given respectively by the following equations:

$$i_k^c = \sum w_{jk}^B c_k o_{jk}^B \quad (1)$$

$$o_k^c = f(i_k^c) \quad (2)$$

and

$$f(s) = (e^s - e^{-s}) / (e^s + e^{-s}) \quad (\text{intermediate level}) \quad (3)$$

$$f(s) = 1 / (1 + \exp(-s)) \quad (\text{output level}) \quad (4)$$

That  $f(s)$  of the output level outputs values of fixed sign as in Equation (4) is due to the fact that in tracking the target, if upward tracking is carried out by contracting the actuator 1 and downward tracking is carried out by contracting the actuator 2, the device is elongated due to its mechanism every time tracking is performed, and approach to the target becomes possible. For updating the coupling weight use was made of the method of backward propagation of errors.<sup>4</sup> In this study with squared error defined by

$$E = (l^2 + d^2) / 2 \quad (5)$$

the coupling weight is corrected according to

$$w_{new} = w_{old} + \Delta w \quad (6)$$

$$\Delta w = -\mu \nabla_w E \quad (7)$$

Now, let the target position and the docking mechanism position be given by  $y' = (x_d, y_d)^T$  and  $y = c(x) = (x, y)^T$ , respectively, where  $x$  is the actuator variable and  $c(x)$  represents the kinematics of the structure. In this case, the squared error in Equation (5) becomes

$$\begin{aligned} E &= (1/2) ((x_d - x)^2 + (y_d - y)^2) \\ &= (1/2) (y' - c(x))^T (y' - c(x)) \end{aligned} \quad (8)$$

and  $\nabla_w E$  in Equation (7) becomes

$$\begin{aligned} \nabla_w E &= -(\partial / \partial w) c(x)^T (y' - c(x)) \\ &= -(\partial x / \partial w)^T (\partial y / \partial x)^T (y' - c(x)) \end{aligned} \quad (9)$$

### 3. Learning of the Controller

First, rendezvous with a fixed target is learned. Learning proceeds with the horizontal distance between the target and the docking mechanism kept at a constant value by elongating the actuators (1) and (2) of the shear deformation module by predetermined lengths, and gradually increasing the vertical distance. Trial is continued while changing the coupling weight, and the target position is changed when the deviation  $d$  is made small to a certain extent.

After completion of learning about a fixed target, a sinusoidal oscillation  $y = \pm A \sin(\omega t)$  is given to the target, and it is tracked.

The tracking situation by the controller in the final stage of learning is shown in Figure 3. The sinusoidal oscillation given to the target has  $A = 7.0$  mm and  $\omega = 0.05$ . The abscissa is the operating time, and the ordinates are the  $y$  coordinate  $y_d$  and the deviation  $d$  of the target. The deviation  $d$  and the distance  $l$  after the completion of the control are indicated in absolute value in the graph.

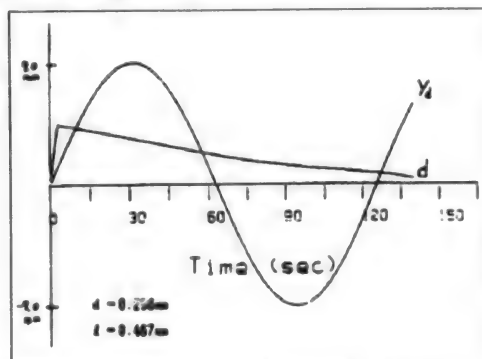


Figure 3. Tracking and Rendezvous by Means of a Controller in Learning (amplitude 7.0 mm, period 125 sec)

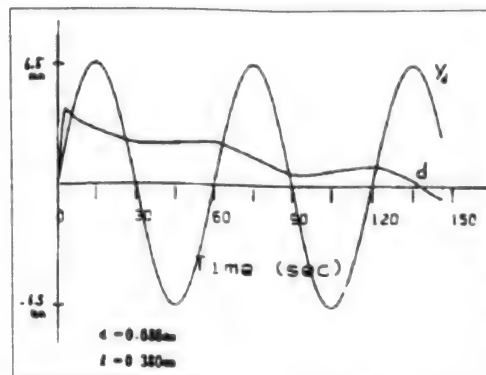


Figure 4. Tracking and Rendezvous by Means of a Controller After Completion of Learning (amplitude 6.5 mm, period 60 sec)

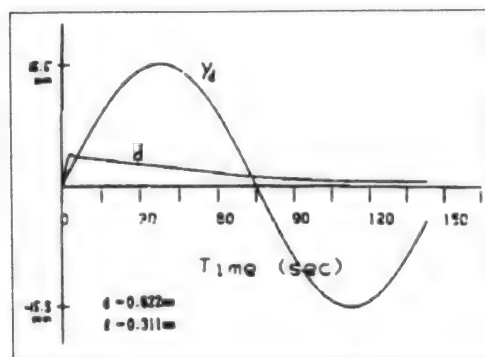


Figure 5. Tracking and Rendezvous by Means of a Controller After Completion of Learning (amplitude 15.5 mm, period 150 sec)

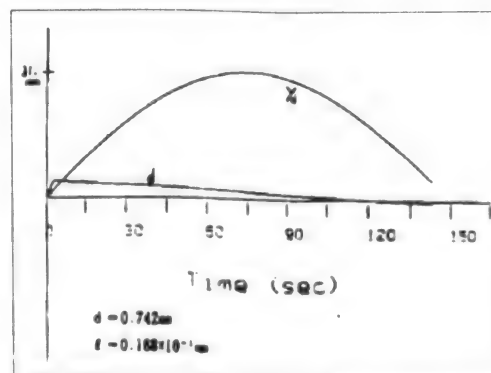


Figure 6. Tracking and Rendezvous by Means of a Controller After Completion of Learning (amplitude 31.0 mm, period 300 sec)

#### 4. Tracking and Rendezvous Using the Controller After Learning

After completion of learning, tracking and rendezvous were carried out by fixing the coupling weight and changing the target motion. Figures 4 to 6 show the results of tracking and rendezvous with the targets to which are given sinusoidal oscillations with amplitudes 6.5, 15.5, and 31 mm, and periods 60,

150, and 300 seconds, respectively. For the target with the period 60 seconds, tracking is insufficient. In contrast, for the target with the period 300 seconds, considerably good results are obtained.

## 5. Conclusion

A neural network was applied to tracking and rendezvous of targets by means of simulation of the two-dimensional truss space structure, and succeeded to some extent in tracking and rendezvous with targets having oscillations that are different from the target used at the time of learning. The task for the future is the combined study of tracking and rendezvous of higher precision and control which reduces the impact at the time of docking, in order to realize soft docking.

## References

1. Matsuzaki, Y., Furuya, H., Kuwao, F., and Takahara, H., "Docking/ Separation of Two-Dimensional Truss Structure With Variable Geometrics," AIAA Paper No. 90-0945-cp, 1990.
2. Matsuzaki, Y., Hosoda, H., and Hayakawa, Y., "Application of Fuzzy Control to Tracking for Docking Operation of an Adaptive Space Structure," Proceedings of the First Joint U.S./Japan Conference on Adaptive Structures, Technomic Lancaster, USA, 1991, pp 792-803.
3. Matsuzaki, Y. and Hosoda, H., "Application of Fuzzy Control to Tracking and Rendezvous Test for Docking of an Adaptive Space Structure," AIAA Paper No. 91-1234, 1991.
4. Lamelhardt, D.E., translation edited by S. Amari, "PDP Models," SANGYO TOSHYO, 1989.

## **Application of Light Aircraft Structure Design To High-Speed Train Body Structure**

936C1015C Tokyo KOZO KYODO NI KANSURU KOENKAI in Japanese 15 Jul 92 pp 42-45

[Article by Kanya Koga, Yoshiharu Noguchi, and Hisao Shikuwa, Mitsubishi Heavy Industries, Ltd., and Kazuhiro Igarashi and Shiro Hosaka, Central Japan Railway Company]

[Text] **Abstract:** In recent years, the need for high speed is increasing in railway transportation, and development of rolling stock having excellent lightweight, high-strength, high-rigidity, and high-fatigue resistance qualities is becoming important. For the rolling stock on the Yamanashi experimental railway now under development, application of lightweight structure technology is especially indispensable also from its running system of magnetic levitation. A brief description of experimental body structure of ultralightweight rolling stock to which the technology of lightweight aircraft design is applied, and the result of load tests will be given in this article.

### **1. Introduction**

In recent years, the need for high speed is increasing in railway transportation, and development of rolling stock having excellent lightweight, high-strength, high-rigidity, and high-fatigue resistance qualities is becoming important. These needs are the same as those necessary for the light structure design of aircraft, and it is especially indispensable to apply the lightweight structure technology to the rolling stock on the Yamanashi experimental line currently under development from its magnetic levitation running system. In this article, we will give a brief report on the body structure of linear motor cars, implemented over FY90 and FY91 by Mitsubishi Heavy Industries, Ltd., based on joint development with the Central Japan Railway Co., and experimentally designed and manufactured to satisfy the structural requirements of railway rolling stock while applying the design and analysis technology/working technology for a light aircraft structure, according to the so-called aircraft structure base. We will also give a report on the result of a static load test given on the motor car.



## 2. Initial Design Study

### 2.1 Fundamental Specifications and Load Conditions

The fundamental dimensions, the fundamental performance, and the load conditions were set by Central Japan Railway Co. by considering the conditions for the rolling stock system as a whole, such as passenger transporting capability, running stability, riding comfort, weight distribution, etc. The principal items are listed in Table 1.

Table 1. Basic Specifications of Trial Manufactured Body Structure

1. Dimension (Unit: mm)	
Length of car	: 24,300 (body structure 23,700)
Width of car	: 2,900
Maximum height of body structure	: 3,100
Window size	: 300 x 400 (opening size 340 x 440)
Entrance size	: 700 x 1,800 (opening size 870 x 2,090)
2. Basic performance	
Weight	: $\leq 2,200$ kg (target value)
Equivalent flexural rigidity	: $\geq 1.2$ GNm <sup>2</sup> (target value)
Natural frequency of flexure	: $\geq 10$ Hz (for body structure before outfitting)
Torsion rigidity	: For the state with crew on board (to be less than prescribed value under three-point support condition)
3. Loading condition	
Vertical load	: 189 kN (including self-weight of body structure, equipment and passengers)
Car end compressive load	: 392 kN (with simultaneous loading of vertical load of 120 kN)
Torsional load	: $\geq 39$ kNm
Maximum airtight load	: Pressure outside car -20~+13 kPa

### 2.2 Materials Used and Selection of Connection (Assembly) System

The fatigue strength characteristic of representative light aluminum alloy materials used for the fuselage structure of aircraft and the existing rolling stock body structure is shown in Figure 1. There is seen a big difference between the rivet connection of high-strength aluminum alloys for aircraft and the welding connection of aluminum alloys for railways. Accordingly, in order to realize light weight and to develop high-strength, high-rigidity, and high-fatigue resistant body structures, we decided to use high-strength aluminum alloy materials for aircraft and adopt assembly system by rivet connection to realize marked reduction in weight.

### 3. Detailed Design/Manufacture and Weight Measurement

#### 3.1 Preparation of Manufacturing Chart

A detailed design was obtained based on the initial investigation in section 2, and a manufacturing chart was prepared. A schematic structural diagram is given in Figure 2.

#### 3.2 Strength Analysis and Natural Frequency Analysis

For the manufacturing chart in Section 3.1, strength was investigated by the finite element method (FEM) analysis. Natural frequency analysis was carried out using the FEM model. The FEM analysis model and the result of the frame bending moment analysis are given in Figures 3 and 4, respectively.

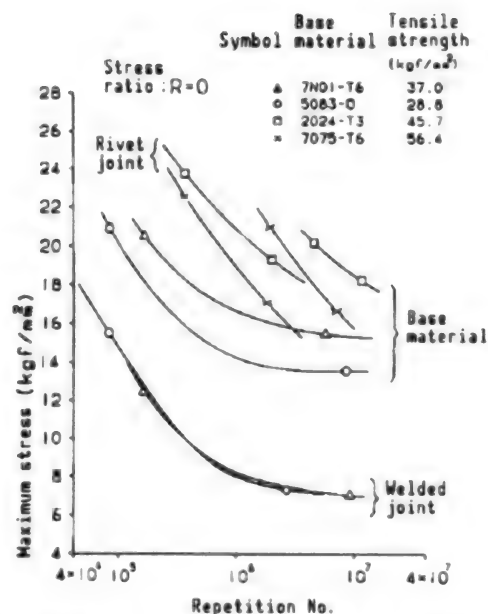


Figure 1. Aluminum S-N Diagram

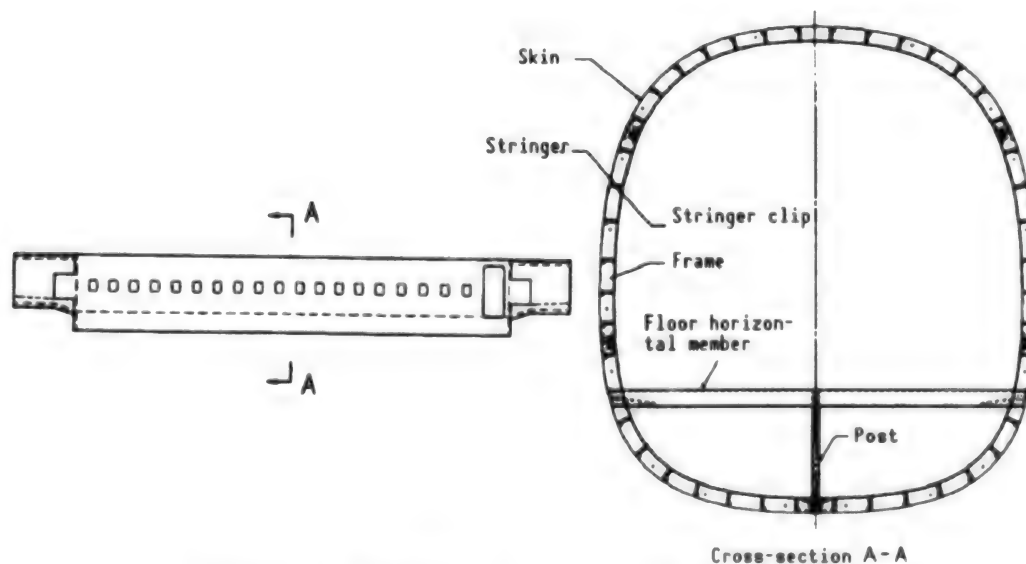


Figure 2. Schematic Diagram for Structure

#### 3.3 Manufacture of Body Structure/Weight Measurement

Based on the manufacturing chart in Section 2.1, a body structure with extremely satisfactory dimensional accuracy, appearance, and showiness was completed as shown in Figure 5 by using simple jigs.

The actual measured weight was 2,036 kg against a target weight of 2,200 kg, accomplishing a weight reduction of 7.5 percent.





Figure 3. FEM Model

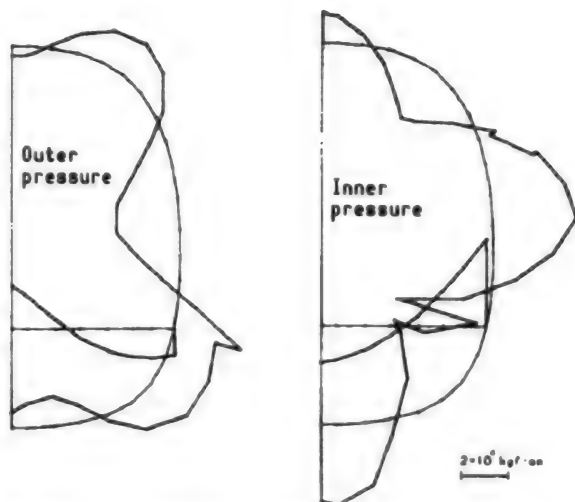


Figure 4. Moment of Bending of Frame in General Part: Airtight Static Load Test



Figure 5. Overall Photograph of Body Structure

#### 4. Load Test

##### 4.1 Items and Method of Test

The load tests were done in accordance with "Load Test Method for Railway Rolling Stock Body Structure." Test items and the loading order are shown in Table 2.

##### 4.2 Load Test

The load tests were carried out according to Table 2. Throughout the tests this body structure required no modification and withstood the test loads and confirmation of the strength and acquisition of sufficient data were possible. The test situations, etc., are shown in Figures 6 to 9.

**Table 2. Items and Order of Tests**

	Test item	Loading condition	Specified value
1	Vertical load test	Riding capacity car weight multiplied by dynamic coefficient 1.1	189 kN
2	Car end compressive load test	Simultaneous loading of car end compressive load and vertical load	Compression: 392 kN Vertical: 120 kN
3	Three-point support test	Riding capacity car weight	173 kN
4	Flexural natural frequency measuring test	—	$\geq 10$ Hz Body structure before outfitting
5	Torsional load test	Torque loading at air spring position with one end fixed	$\geq 39$ kNm
6	Airtight static load test	Static loading of external and internal pressures	Internal: 20 kPa External: 13 kPa

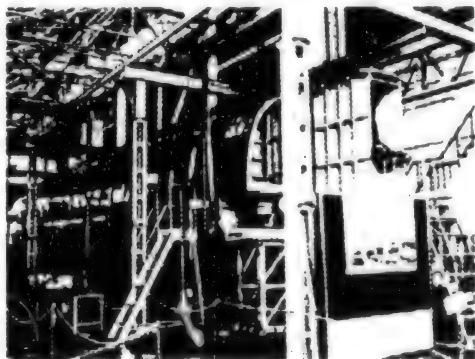


**Figure 6. Vertical Load Test (1/2)**

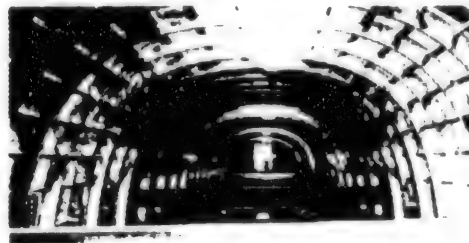


**Figure 7. Vertical Load Test (2/2)**

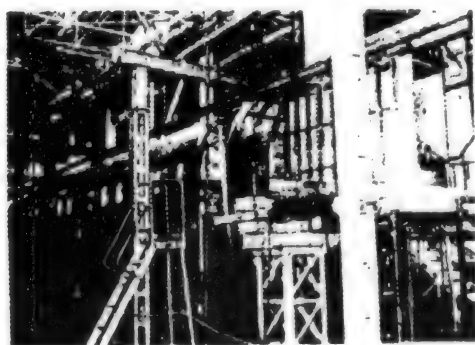


**Figure 8. Car End Compression Test**

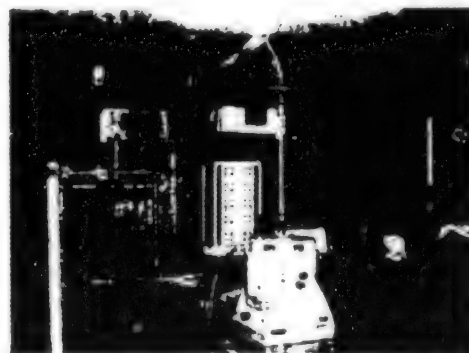


**Figure 9. Test Equipment Setup and Excitation Device**

#### **1) Vertical load test**

The body structure withstood the test load, and there was generated no inconvenience such as permanent deformation after removal of the load. When the load exceeded the maximum by 40 percent, the outside sheet of the cabin ceiling part started to buckle. This buckling decreased gradually in the course of removal of the load, disappearing completely after removal of the load, confirming that it was an elastic buckling.

#### **2) Compressive load test on body end**

The body structure withstood the load, and there was generated no permanent deformation after removal of the load.

#### **3) Three-point support test**

The body structure withstood the load, and there was generated no permanent deformation after removal of the load. In the state of three-point support, the outside sheet in the upper part of the entrance was buckled, but this buckling decreased in the course of removal of the load and disappeared completely after removal of the load, confirming that it is an elastic buckling.

#### **4) Measurement of natural frequency of flexure**

The first order natural frequency of flexure was 11 Hz, and the second order natural frequency of flexure measured for reference was 42.7 Hz.

#### **5) Torsion load test**

The body structure withstood the load, and no inconvenience, such as permanent deformation after removal of the load, was generated.

#### **6) Static airtight load test**

The body structure withstood the test load for internal pressure and external pressure, and no inconvenience, such as permanent deformation, was generated.

### **4.3 Analysis and Evaluation of Test Results**

The overall evaluation of the various load tests in Section 4.2 is that the measured stress at each load test was not too high, and agreed fairly well with the analytical stress. A comparison between the measured stress in the test and the analytical stress is shown in Figures 10 to 12. An analytical evaluation of the test results is summarized in Table 3. Except for a few items to be improved there was no problem in terms of strength, confirming that the design of the experimental body structure was fully acceptable.

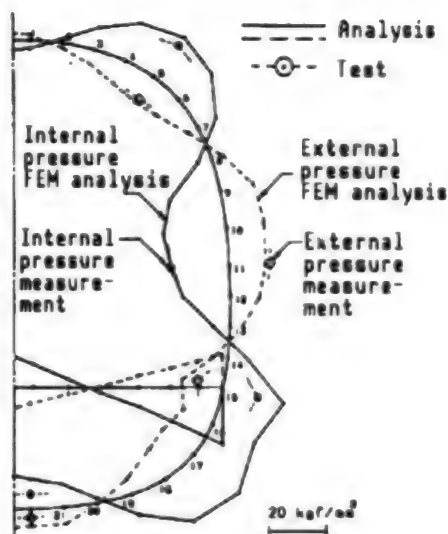


Figure 10. Frame Stress Comparison: Airtight Static Load Test

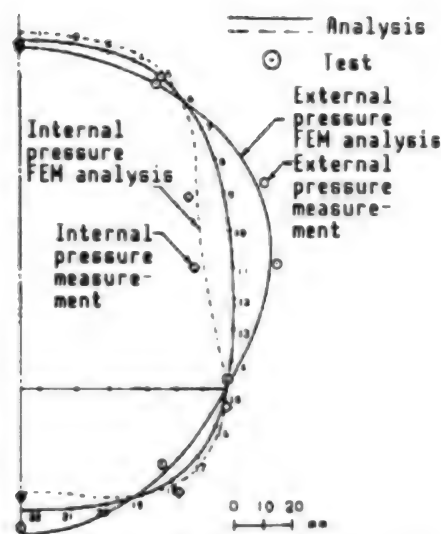


Figure 11. Frame Displacement Comparison: Airtight Static Load Test

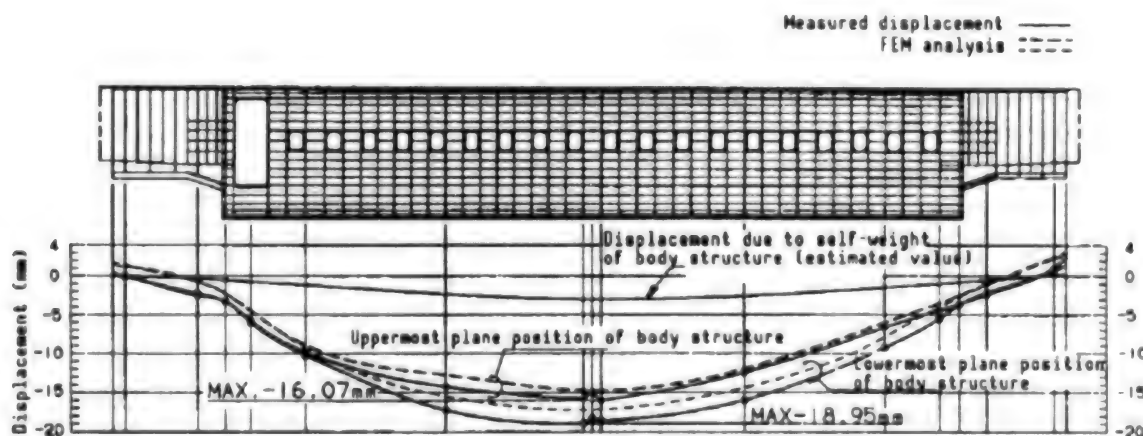


Figure 12. Displacement Diagram for Vertical Flexure: Vertical Load Test

## 5. Conclusion

Based on the lightweight aircraft structure design technology, the so-called aircraft structure-based design/manufacture/test of an experimental body structure which pays sufficient attention to indispensable matters as railway rolling stock (linear motor car) were carried out.

The measured weight achieved a weight reduction of 7.5 percent of the target weight, and body structure withstood the loads throughout the tests without requiring any modification, permitting us to confirm the strength and to acquire sufficient data. From the above results, the validity of design and manufacture of the body structure on the aircraft structure base was demonstrated, and the feasibility of a lightweight, high strength, and high-rigidity rolling stock was confirmed. It is now important to confirm the fatigue strength and durability by performing the airtight load repeated test.

Table 3. Summary of Analytical Evaluation of Test Results

Test item	Criterion for evaluation of JISE7105	Result of load test	Analytical evaluation
1 Vertical load test	Stress does not exceed yield point or bearing force of material	Over 40% load weight buckling generated in skin of ceiling part	Stress level low, no problem with respect to strength
2 Car and compressive test	" " "	Slight residual strain generated in skin of ceiling part	No problem if improvement to fixing position of linking part when position determined
3 Three-point support test	No generation of permanent deformation and plastic buckling	Elastic buckling generated in skin of ceiling part and in entrance upper part	Has sufficient strength
4 Flexural natural frequency measuring test	Not less than 10 Hz for body structure before outfitting	11.0 Hz (includes 320 kg of floor board for load)	Positively satisfies required value
5 Torsional load test	Stress does not exceed fatigue limit of material	Maximum stress of supporting beam of 26.4 N/mm <sup>2</sup> , angle of torsion $9.05 \times 10^{-5}$ rad/m	Stress sufficiently low, no problem with fatigue strength
6 Airtight load test	" " "	Measured stress generally low, mostly agreeing with analytical stress	Agreement with analytical stress good, validity of fatigue design confirmed

## **Strength Properties of Oxidation Resistant Three-Dimensional-Fabric/Ceramic Superhigh Temperature Composites**

936C1015D Tokyo KOZO KYODO NI KANSURU KOENKAI in Japanese 15 Jul 92 pp 162-165

[Article by Takashi Ishikawa, Yoichi Hayashi, Yoshio Noguchi, and Masamichi Matsushima, Airframe Division, National Aerospace Laboratory; Takemi Yamamura, Ube Industries, Ltd.; and Tetsuro Hirokawa, Shikibo, Ltd.]

[Text] **Abstract:** Oxidation-resistant superhigh-temperature ceramic composites are developed. Reinforcement is three-dimensional woven fabrics where Si-Ti-C-O fibers are utilized. Matrix filling is done by two methods: polymer conversion and chemical vapor infiltration (CVI). Strength at room temperature exceeds French SEP data by 20 percent and strength at 1,200°C is 90 percent of room temperature value, so far. Future strength increases seem to be possible.

### **1. Introduction**

The National Aerospace Laboratory, together with Ube Industries, Ltd., and Shikibo, Ltd., has been engaged in research and development of superhigh-temperature composites obtained by charging a three-dimensional fabric using Si-Ti-C-O fiber (tradename: Tyranno) with a ceramic base material, as a heat-resistant material which has far superior oxidation resistance and strength comparable to the currently available C/C materials for structural materials or engine materials for future spaceplanes.<sup>1</sup> In this report we will present the results of the normal temperature static strength characteristic test and a preliminary high-temperature strength characteristic test of this material. Traditionally, a French company SEP has used SiC fibers to develop a two-dimensional fabric reinforcing material/CVI method SiC matrix material. Strength of the new material at normal temperature exceeds that of the already available material by about 20 percent. In addition, the strength at high temperature is about 90 percent of the room temperature value.

### **2. Materials Tested**

The reinforcing fiber of this material is an Si-Ti-C-O fiber which is woven into an orthogonal three-dimensional fabric. The three-dimensional fabrics can roughly be classified<sup>2</sup> into the two kinds of woven fabric shown in Figure 1 and the braided material. But in this study we used two kinds of reinforcing fabrics, SCL and SC, that belong to the orthogonal woven fabric system shown



in Figure 1(a). Cross-sectional photographs of composites, SCL04 and SC04, of chemical vapor infiltration (CVI) method matrix with the orthogonal three-dimensional structure are shown in Figures 2 and 3, respectively. The total  $V_f$  is about 40 percent.

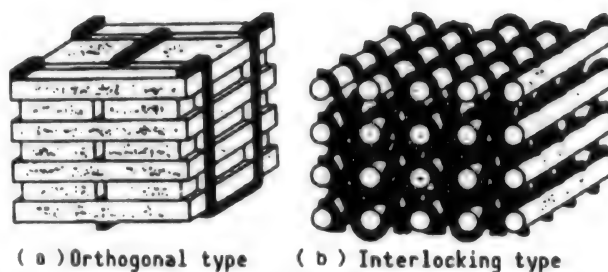


Figure 1. Examples of Orthogonal Three-Dimensional Fabric

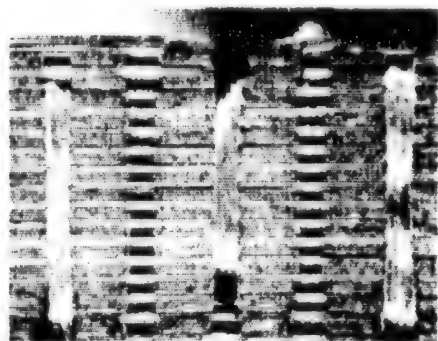


Figure 2. Cross-Sectional Photograph of Specimen SCL04 Produced by CVI Method

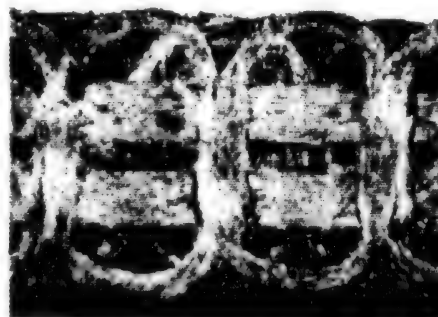


Figure 3. Cross-Sectional Photograph of Specimen SC04 Produced by CVI Method

The dimensions (in mm) of the woven three-dimensional fabric preforms are nominally  $240 \times 240 \times 6^t$  and  $240 \times 150 \times 6^t$ . These are charged with a ceramic base material. The following two methods for charging were used. The first is the method in which polytitanocarbosilane organic material resembling a fabric precursor is impregnated and firing is repeated to obtain a product similar to a C/C material. In this processing, six kinds of plate-form composite molds, SC01-SCL03, were trial manufactured for the three systems, in combination with the fabric, by varying the surface treatment of the fabric and the kind of precursor organic material. The second method is a chemical vapor infiltration (CVI) method which is assumed to be analogous to the method employed by SEP Cie. in France. This is a method in which silane gas is used, and an SiC phase is deposited in the interior of the preform by thermal decomposition. By giving an identification number 04 to the products, two baseboards SC04 and SCL04 were trial manufactured. Accordingly, a total of eight kinds of molds were obtained.

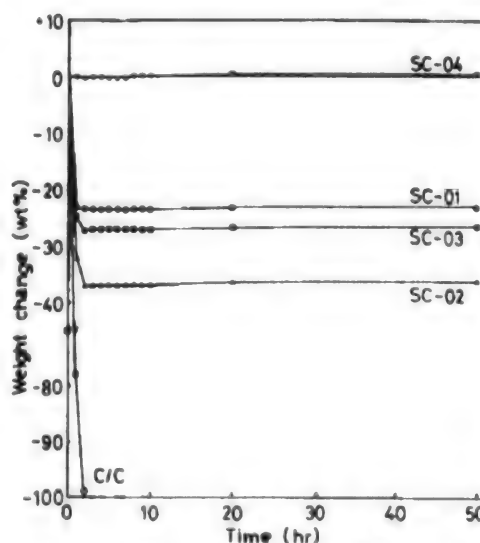


Figure 4. Comparison of Weight Change of This Material and C/C in Atmosphere at  $1,000^{\circ}\text{C}$

The most significant feature of this material is that it has an extremely low oxidation rate compared with the C/C materials. As shown in Figure 4, the rate of weight reduction of 04 in static atmosphere at 1,000°C is 0, and the reduction rate for 01-03 is 0 beyond a certain saturation point, which shows that it is far superior to the C/C materials. Moreover, such a difference in the rate of oxidation is expected to be amplified further in a field of large flow speed. Further, the specific gravity of this material is a small value of about 1.7.

### 3. Machining of Specimens

A strip board of nominal width 25 mm was segmented from the composite plate using a diamond cutter, and dumbbell shaped specimen as shown in Figure 5 was machined by a copying jig. The machining was done by NAL. Since this composite matrix is very hard and difficult to cut, there were several problems in cutting and machining. In the application of this material in the future it will become necessary to examine the problem of machining starting with the early stage.

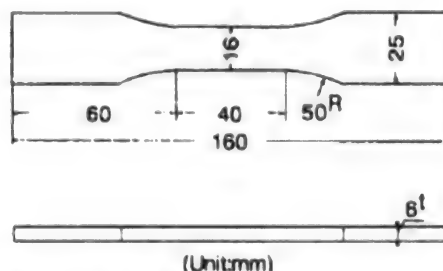


Figure 5. Shape and Dimensions of Specimen at Normal Temperature (Nominal value)

### 4. Strength Test at Normal Temperature

A strength test at normal temperature of specimens segmented from the eight kinds of mother-board was performed using Instron 8501. Using a hydraulic grip the specimen was gripped via a thick paper to prevent collapse of the specimen surface. This mechanism functioned satisfactorily without causing slip. The test mode chosen was displacement control, and the displacement was set to be 0.5 mm/min. Since the strain gauge cannot be used for strain measurement because of the indentation and the surface property, a clip gauge with gauge length of 25 mm was used. In addition, anisotropic elastic (AE) measurement was performed for some specimens in order to obtain data to be used for the analysis of the nonlinear behavior. Apparatus used for this purpose are SPARTAN-AT and TRA

2.5 system. The state in which a specimen is mounted on the testing machine, and a clip gauge and the AE sensors attached, is shown in Figure 6. The upper and the lower sensors on the left flank are for one-dimensional position location, and the sensor in the upper right is for frequency analysis. During the AE measurement, cycles of application and removal of a load before fracture were given to some specimens according to reference 3.

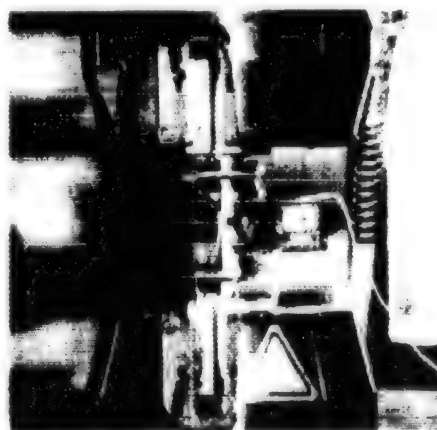


Figure 6. Setup of Normal Temperature Test (Note the clip gauge AE sensors)



## 5. Representative Result of Strength Test at Normal Temperature and Consideration

As representative examples of the result of strength at normal temperature, the load (stress)-strain curve is shown in Figures 7 and 8 for specimens that showed maximum value in the CVI and polymer conversion (PC) methods, respectively. As shown in Figure 7, the CVI product shows the strength of 242 MPa which exceeds the strength of the two-dimensional fabric reinforced material (CVI) of SEP Cie.<sup>4</sup> In SCL04, the average value for four specimens was 226 MPa which exceeds the SEP value, and the scatter of the data is relatively small. Among the specimens by the PC method which is estimated to be advantageous from the viewpoint of manufacturing cost there was one specimen that has high strength as shown in Figure 8. The potential of the method can fully be recognized, but the properties of the products are by no means uniform, so it is considered necessary to improve the method of molding.

Furthermore, this material is clearly superior to the SEP materials in nonlinearity starting strain, rupture strain, etc., in addition to the strength. In contrast to the case of the SEP materials whose quality is nearly settled, this material is in the initial stage of development and its strength is being increased rapidly. Therefore, it should be added that improvement of the strength in the near future can be expected to some extent.

## 6. Example of Acquired AE Data

For some specimens AE data was obtained as mentioned above. First, the AE history, when load removal/loading cycles are given for the purpose of acquiring the rupture toughness index in a simple way, following reference 3, is given in Figure 9, and the stress-strain behavior at that time is given in Figure 10. The specimen is SCL01 of PC product, and it shows the result for pulling in the lateral (y) direction. These results including the AE behavior show a tendency similar to the result of the two-dimensional SiC/SiC material made by SEP shown in Figure 6 of reference 3. However, superiority of this material in the nonlinearity

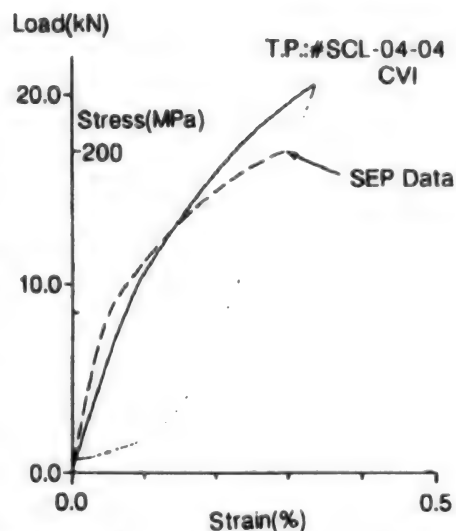


Figure 7. Load (Stress)-Strain Curve for Highest Strength CVI Product

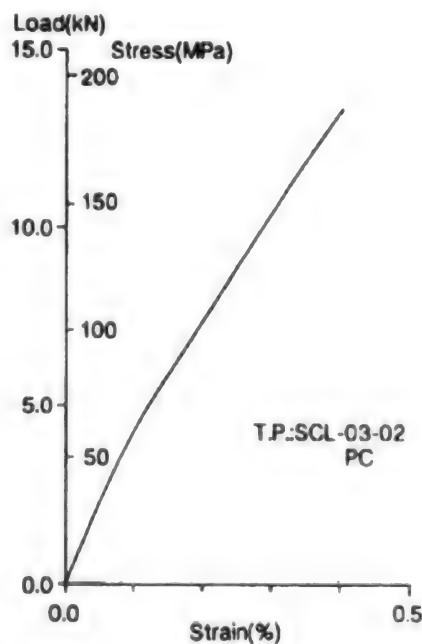


Figure 8. Load (Stress)-Strain Curve for Highest Strength PC Product

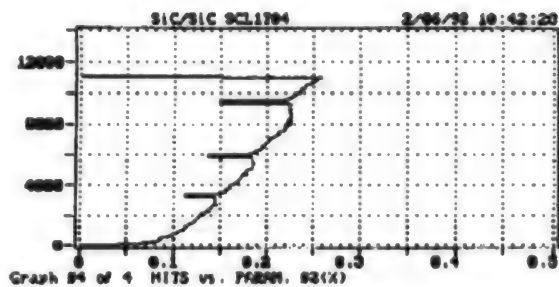


Figure 9. Example of AE Data for Load and Unload Cycles  
(abscissa: strain, ordinate: Hit)

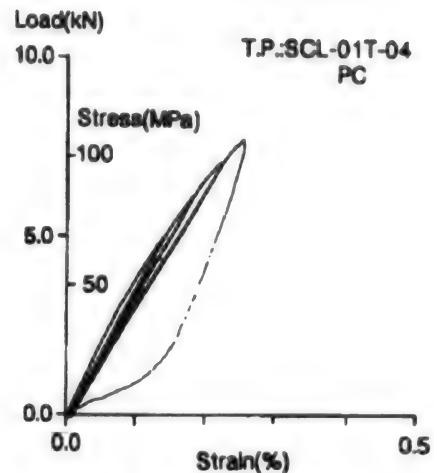


Figure 10. Load (Stress)-Strain Curve for Figure 9

starting strain, residual strain, etc., can be recognized. It should be noted that the plot at the time of removal of the load is not showing the load removal process completely for the convenience of the drawing software. Next, the case of AE measurement at the time of testing of the maximum strength specimen shown in Figure 7 is given in Figure 11. This AE property and the nonlinear behavior are curious at a glance from the analogy of the lateral crack behavior of carbon fiber-reinforced plastic (CFRP), but reproducibility of these behavior exists for the SCL04 group. The elucidation of these properties related to the growth of microcracks is an important future research problem.

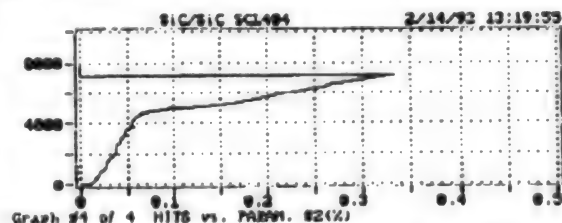


Figure 11. Example of AE Measurement for SCL04-04 (Product with highest strength)

## 7. Orthogonally Anisotropic Elastic Characteristic

This material exhibits anisotropy since it uses an orthogonal three-dimensional fabric as a reinforced material. It is necessary to roughly grasp this characteristic before proceeding to future research. From the orientation ratio of the fiber of the reinforcing fabric it can be estimated that SC will have greater anisotropy than SCL, and the result of a trial experiment supports this view. Figure 12 shows the anisotropic elastic characteristic of SC03. The basic values used for calculating this figure are the following five: elastic coefficients  $E_L$ ,  $E_T$ , and  $E_{45}$  measured in the region up to the strain of 0.5 percent, and  $\nu_L$  and  $\nu_{45}$  obtained by carrying out only the Poisson ratio measurement (details are

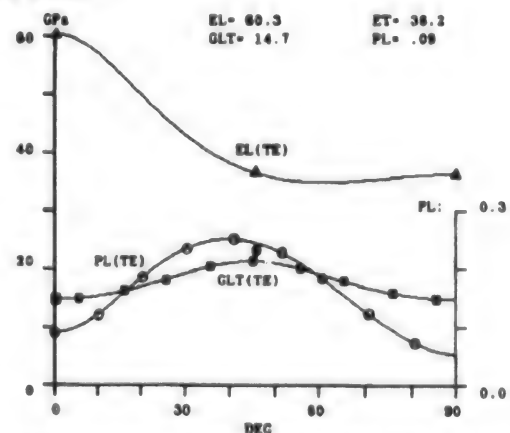


Figure 12. Anisotropic Elasticity of SC03 (Calculated value using principal axis value)

omitted) on the specimen prior to the dumbbell machining. Using these data  $G_{LT}$  was determined according to the well-known relationship between  $E_{45}$ ,  $\nu_{45}$ , and  $G_{LT}$ . A mutual calibration in terms of  $\nu_L$  without the use of  $\nu_{45}$  is also possible. In this way, the four independent elastic coefficients of the two-dimensional orthogonally anisotropic material were determined, and the curves shown in Figure 12 were calculated using these coefficients.

#### 8. Result of Preliminary High-Temperature Test and Consideration

A part of high-temperature tests up to 1,200°C was carried out for this material using the superhigh-temperature static strength testing device introduced to the National Aerospace Laboratory. This temperature is determined by the tolerable temperature of a jig employed in the testing system in which the metallic jig is placed in the heating part. The situation in which the specimen is set in the heating part is shown in Figure 13. The tensile force is introduced from the jig to the specimen shoulder. The shape of the specimen for high-temperature test designed to match the jig is shown in Figure 14.

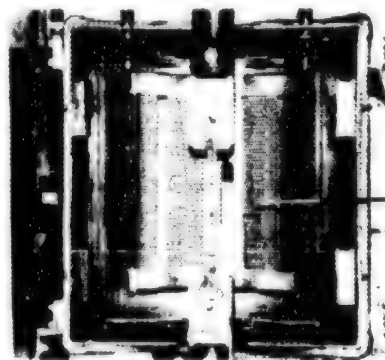


Figure 13. Setup for High Temperature Test Using Heating Part Insertion Type Jig Made of Molybdenum Alloy

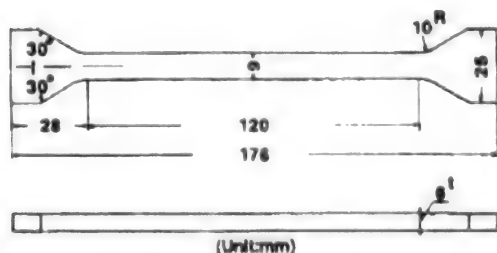


Figure 14. Specimen for High Temperature Tensile Test

A ceramic paper (made by Taiyo Chemical Co.) is inserted to improve the contact between the contact surface of the specimen shoulder and the jig. The strength of the CVI products, SC04 and SCL04, at 1,200°C and 1,150°C, and the normal temperature strength of a fiber single body to be used as reference are given in Figure 15. The specimen SC04 was broken at the parallel part, but SCL04 first underwent shearing fracture at the gripping part for both specimens as shown in Figure 16, so its tensile strength is considered to be greater than the data shown in the graph. Even if one assumes that this data is the correct one, the strength at 1,200°C is 90 percent that at normal temperature. It is scheduled to continue the test by improving the shape of the specimen.

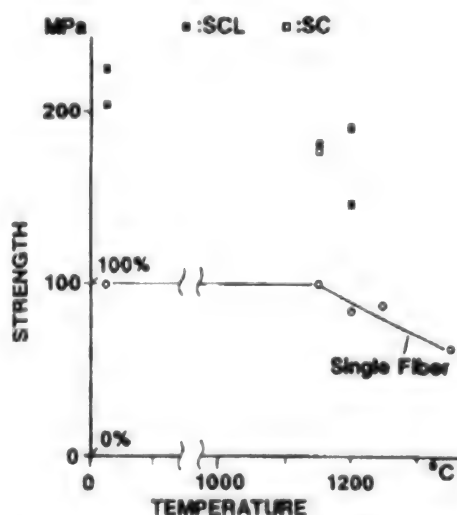


Figure 15. Preliminary Result of Static Tensile Test at High Temperature

## 9. Evaluation at the Present Time

Although it is still in the initial stage of development, the present material (CVI product) has normal temperature strength that exceeds considerably that of the precedent similar material, namely, the two-dimensional SiC/SiC material by SEP Cie. and exhibits excellent high-temperature strength. The PC product of this material also shows the potential for high strength. We are planning to realize further improvement of the strength of this material, and carry out research and development aimed at its application to the H-II orbiting plane (HOPE), etc.

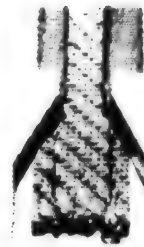


Figure 16. Shearing Fracture at High Temperature Test of SCL04

## References

1. Ishikawa, T., Abstract of papers for 30th Space Science and Technology, 1986, p 32.
2. Goetze, R.H., et al., Leading Edge, GE Report, 1988.
3. Bouquet, M., et al., COM. SCI. TECH., Vol 37, 1990, p 223.
4. Choury, J.J., 1st Int. FGM Symp., 1990, p 157.

## **Ultrasonic NDI Results for C/C, CF/Polyimide Composite Components**

936C1015E Tokyo KOZO KYODO NI KANSURU KOENKAI in Japanese 15 Jul 92 pp 202-205

[Article by Masamichi Matsushima and Takashi Ishikawa, National Aerospace Laboratory; and Yoshiki Morino, National Space Development Agency]

[Text] **Abstract:** Ultrasonic flaw detection test using multichannel flaw detection, etc., was performed on composite components to be used for spaceplanes, and the result was compared with the conventional single channel method.

### **1. Introduction**

As a structure for the spaceplane, a design that uses a carbon/carbon (C/C) composite that takes high heat resistance into account for high-temperature parts, and uses carbon fiber (CF)/polyimide composites for heat-resistant structures protected by TPS, is considered promising. For the manufacture of the C/C composite, a method is used in which a cycle of laminating CF fabric, impregnating resin, and baking is repeated. Because of this, the C/C composite becomes essentially porous, and it is necessary to overcome several problems in order to apply the conventional ultrasonic flaw detection method. In this work, flaw detection was carried out by the transmission method that is suited for porous materials, using a robot-type ultrasonic flaw detection device. In addition, multichannel flaw detection which becomes effective when combined with the transmission method was also used. Further, the conventional flaw detection by the reflection method was used for the trial product obtained by the CF/polyimide composite forming method.

In this article the results of these tests will be reported.

### **2. Various Flaw Detection Methods by Robot-Type Ultrasonic Flaw Detection Device**

A brief description of this device was given in a previous report.<sup>1</sup> As shown in Figure 1, there are the following three kinds of flaw detection forms depending upon the characteristics of the specimen and the shape of the members:

1) Local immersion reflection method which is applied to the interior of the surface member, bonded part of the surface member, and the reinforcing material, etc., because of the impossibility of full immersion, when carrying out local flaw detection of the surface of the actual airplane by the ultrasonic echo reflection method.

2) Full immersion reflection method which is applied when the local immersion method is not feasible.

3) Full immersion or water jet transmission method which is applied to honeycomb sandwich structure, etc.

Further, a feature of this device is that there is a multichannel flaw detector (WIND), operation of one to six channels is possible by an indication from the central processing unit (CPU), and a flaw detection of one probe and six channels is possible. In other words, in contrast to the flaw detection by a simple detector in which scanning is repeated several times by changing the sensitivity according to the change in the thickness of the specimen, the sensitivity of one probe in one scanning can arbitrarily be set up to six kinds. Therefore, the device has the capability of carrying out flaw detection with high-time efficiency. When combined with the reflection method that will be described later, the case where the multigain is advantageous is indicated by the mark ●, and the case when it is not particularly advantageous is indicated by Δ in Table 1.

### 3. Application to C/C Plate and T-Type Reinforcing Material

#### 3.1 Inevitability of the Transmission Method

In a previous report<sup>2</sup> we have quantitatively identified the damaged area due to drop impact of CF/EPOXY and CF/polyether ether keton (PEEK) thick plates (48 plies) and a reinforcing plate, by the ultrasonic local immersion

① Local immersion reflection method (mechanical tracking)



② Full immersion reflection method (tracking by teaching)



③ Transmission method (tracking by teaching)

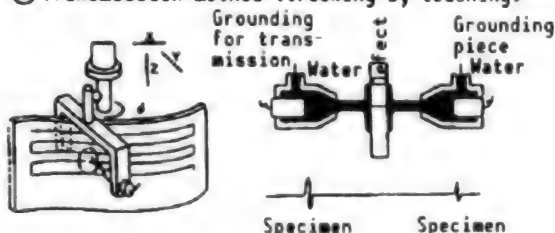


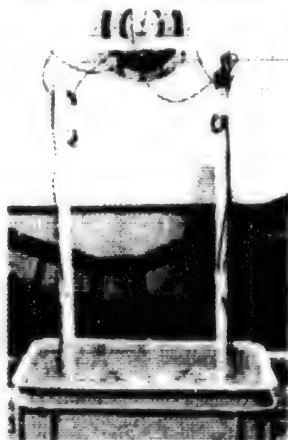
Figure 1. Explanatory Schematic Diagram for Flaw Detection Modes of This Device

Table 1. Flaw Detection Methods and Adaptability of Multigain Flaw Detector

	Single gain	Multigain
Reflection	○	Δ
Transmission	○	●



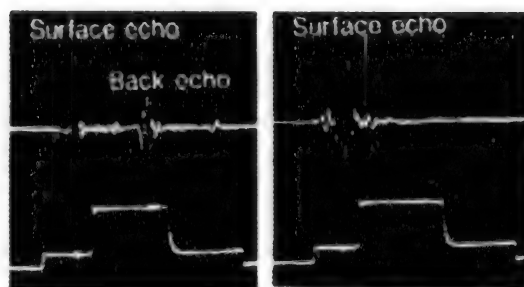
reflection method. In carbon fiber-reinforced plastic (CFRP) with low attenuation as in this case it is possible to judge the back echo as in Figure 2, making the signal processing by the reflection method possible. In contrast, when the reflection method is tried on a porous material such as a C/C composite, it is not possible to obtain an ordinary C scan image because of the disappearance of the back echo due to attenuation of the surface echo as shown in Figure 3.



**Figure 4. Setup for Full Immersion Two-Probe Transmission Flaw Detection**

Since the reflection method is not applicable under these

circumstances, we decided to use a transmission method that uses two probes. The scan pitch of 0.5 mm was adopted, and the flaw detection situation is shown in Figure 4. In addition, an influence of the difference in the attenuation rate for a portion immediately after start of flaw detection and a portion in the latter half of flaw detection will occur even for structurally sound parts if the immersion time is not sufficiently long, since the material is porous. For this reason, flaw detection was given after immersion for more than 12 hours.



**[Left] Figure 2. Echo of Sound Part of CFRP**

**[Right] Figure 3. Reflection Echo From C/C Material**

### 3.2 Examples of Application to C/C Plates

The result of flaw detection by the full immersion method using a multichannel flaw detector, and setting the sensitivity at six different levels (25, 28, 31, 35, 39, and 43 dB) is shown in Figure 5. Two probes with 1 MHz

were used. The C/C plate used is a specimen No. 5 which was compression tested after impact (CAI). Figure 5(1) shows the result of flaw detection with sensitivity 25 dB. It was confirmed that there exists a circular damage mark due to impact on the central part of the specimen and a further damaged region which may have been generated by the compression test. The two vertical black lines in the lower part of the specimen show the lead wires of the strain gauge used in the test, and have nothing to do with the damage. Figure 5(2) is the flaw detection result when the sensitivity is increased by 3 dB from Figure 5(1) and the weaving pattern of the CF cloth is recognizable in the undamaged part rather than the damaged part. The contour of the specimen can most readily be recognized up to sensitivity of 28 dB. Figure 5(3) is the result for 31 dB where the weaving pattern in the sound area can be identified more clearly. Figures 5(4) to 5(6) are the result of varying the sensitivity to 35, 39, 43 dB where only the damage expansion region was confirmed. For sensitivity greater than 39 dB the quality of the image deteriorated. In the specimen (98 x 153 x 2.6 mm) shown in Figure 6, impact damage can clearly be seen, but the damage at the time of the compression test was hardly discernible.

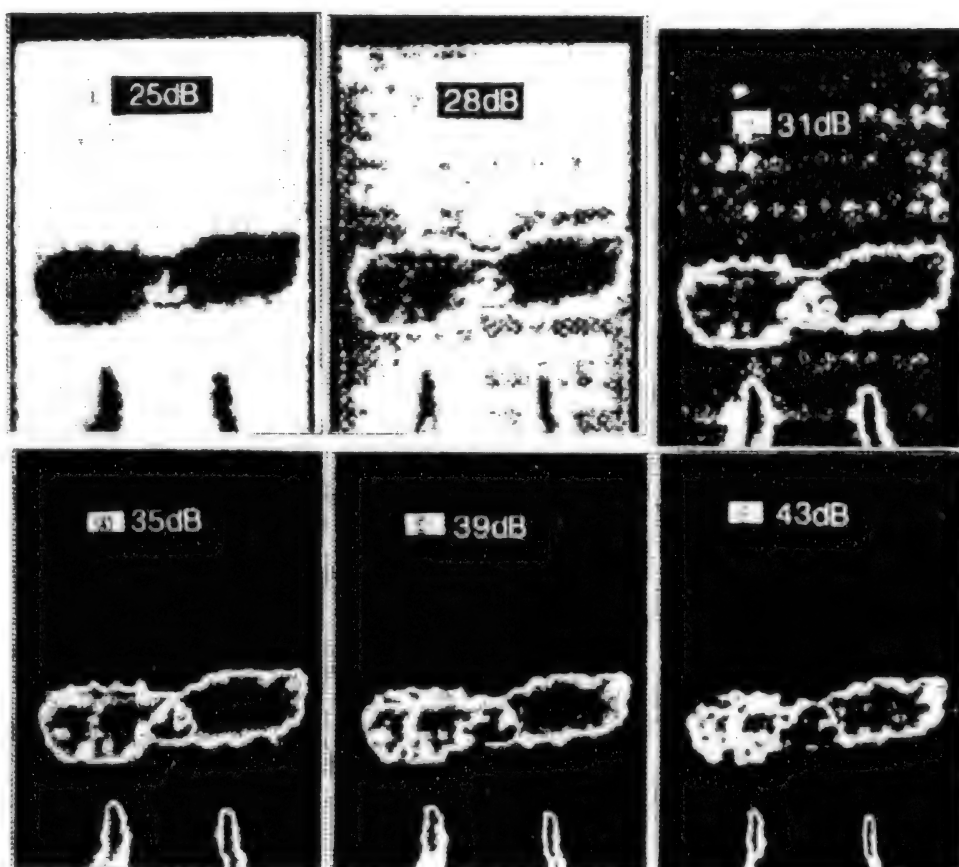


Figure 5. Examples of Using Multigain Flaw Detector  
(25, 28, 31, 39 and 42 dB)



Figure 6.  
Specimen of  
C/C Plate  
(No. 4)

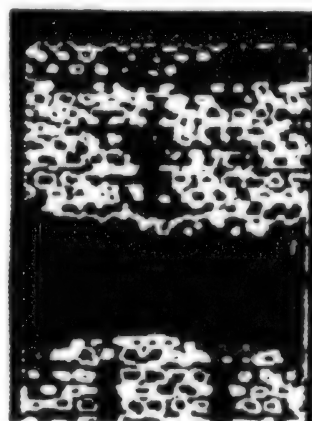


Figure 7. Flaw De-  
tection Result of  
C/C Specimen  
(No. 3)

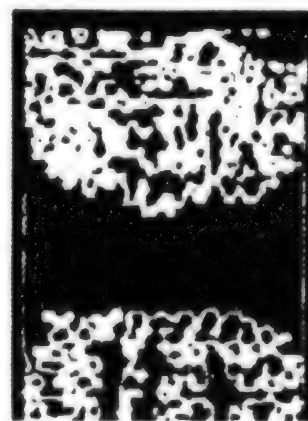


Figure 8. Flaw De-  
tection Result of  
C/C Specimen  
(No. 1)

Figures 7 and 8 show the results for specimens No. 3 and No. 1 for which the multichannel flaw detection was given simultaneously. These also represent the results after the CAI test. For specimen No. 3 (Figure 7) peripheral side damage is clearly recognizable, but for specimen No. 1 (Figure 8) the damage situation cannot be judged visually at all.



### 3.3 Examples of Application to T-Type Reinforcing Material Made of C/C

The specimen is a T-type material after compressive strength test, and due to the peculiarity of the shape, two full immersion transmission tests were given separately for the flange part and the web part. The flaw detection test results for the flange part and the web part are shown in Figures 9 and 10, respectively.

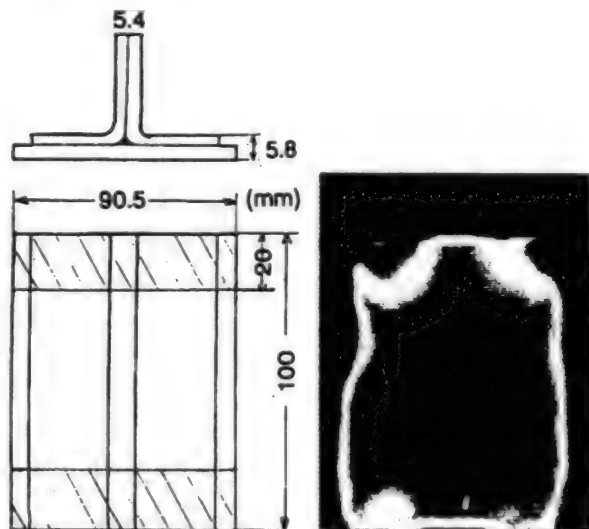


Figure 9. Dimensions of T-Shaped C/C Reinforced Material and Flaw Detection Result of Flange Part (Hatched part is reinforced part at the end)

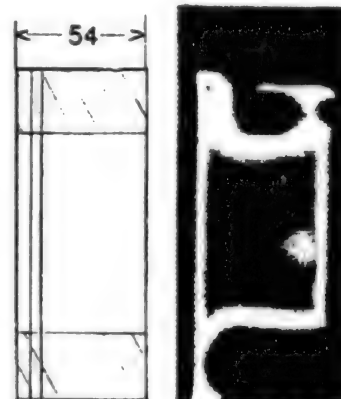


Figure 10. Dimensions of T-Shaped C/C Reinforced Material and Flaw Detection Result of Web Part (Hatched part is reinforced part at the end)

The left side of Figure 9 shows the dimensions of the specimen and the upper and lower reinforcing materials with hatches. In the central area of the specimen rather than the upper and lower parts of the reinforced area, ultrasonic waves cannot pass through the specimen due to aggregation of fine cracks, which is shown in dark color in Figure 9. Figure 10 as well shows the central part in dark color where the ultrasonic wave cannot pass through. The white portion in the center is a crack that was clearly visible. The reason for this may be due to increase in the transmissivity for a crack similar to the case of a hole. At the time of the compression test this T-type reinforcing fiber was bonded at the upper and lower ends to aluminum blocks by potting material. At the time of removal of the aluminum blocks after the compression test, the specimen was heated and its surface was roughened due to residual combusted material of the potting material, which is surmised to have a certain influence in the result.

### 3.4 Examples of Application to CF/Polyimide Composite

The specimen is a trial-formed reinforced plate having four hat-type reinforcing members as shown in Figure 11. It is 800 mm long and 500 mm wide. The flaw detection situation in the local immersion reflection method, is shown in Figure 12. The probe used is of 10 MHz focusing type (20 mm), the sensitivity is set at 28 dB, and the scanning pitch is 0.5 mm.

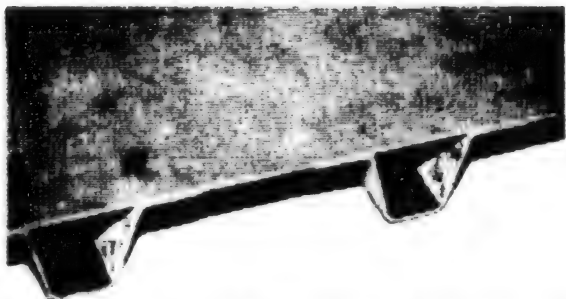


Figure 11. Hat-Reinforced Portions of C/F Polyimide Reinforced Plate

A photograph of the local immersion holder part is shown in Figure 13. The result of the flaw detection thus obtained is shown in Figure 14.



Figure 13. Local Immersion Probe

Since the reflection method was used, the surface member and the bonded part of the surface member and the flange of the hat-type reinforcing member were detected without any problem. Flaws due to some wrinkles on the surface of the specimen can be identified. The result of flaw detection of the surface member and the bonded part shows that this CF/polyimide composite panel has attained a quality which is generally satisfactory.

#### 4. Conclusion

A multigain flaw detection by the transmission method of porous materials represented by C/C material was performed using the multichannel flaw detector installed on the robot-type ultrasonic flaw detection device. The transmission method has to be applied to the porous material, and in so doing, multigain flaw detection by which data with many sensitivities can be obtained in one scan is advantageous. It is considered that fully satisfactory results were obtained for different shapes (plate, T-type material, etc.) and different

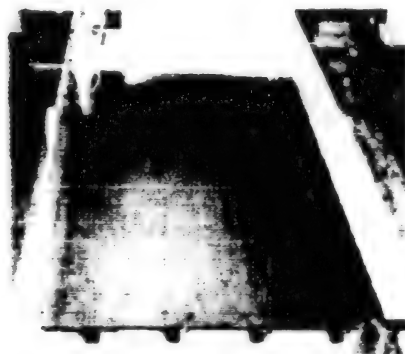


Figure 12. Setup of C/F Polyimide Reinforced Plate



Figure 14. Flaw Detection Result of CF/Polyimide Reinforced Plate

damage situations. In addition, a satisfactory result was obtained for a CF/polyimide reinforced plate in flaw detection by the local immersion reflection method. As in the above, the feasibility of ultrasonic flaw detection, indispensable for strength assurance of structural members for the H-II orbiting plane (HOPE), etc., was made definite by selecting a flaw method suitable for the material and the shape of the specimens.

#### References

1. Matsushima, Ishikawa, and Hayashi, Collected papers for the 33rd Meeting on Structural Strength, 1991, pp 82-85.
2. Matsushima, Hayashi, Ishikawa, and Noguchi, Ibid., pp 288-291.

## **Heat Structural Analysis for Bent, Double-Sided Radiating Heatpipe Type Radiator for HOPE**

936C1015F Tokyo KOZO KYODO NI KANSURU KOENKAI in Japanese 15 Jul 92 pp 206-209

[Article by Masao Furukawa, National Space Development Agency, and Otto Brunner, European Space Agency]

[Text] **Abstract:** A specific frequency analysis at a manual computation level was performed on a bent and double-sided radiating heatpipe type radiator for a spaceplane. The analysis was based on the feeder interval using heat exhaust capability analysis and estimated weight. The result showed that the number of the specific frequency was considerably smaller than what was required. Therefore, the proposal was made to improve the problem of weight increase and to modify the design to some degree in order to compensate for the rigidity.

### **1. Introduction**

The radiator for the space transportation plane HOPE (H-II orbiting plane) now under research and development at the National Space Development Agency (NASDA) has to be attached to the cargo bay door mainly due to equipment design. Accordingly, the radiator for HOPE will have a bent plate-like cross sectional structure; and will be attached in cantilever style to the fuselage cargo bay part. For this reason, the development of the radiator for HOPE requires a heat structural design analysis that takes shape/structure/fitting into account.

### **2. Heat Design**

In general, for the heat design of a radiator it is necessary to know the temperature of equivalent heat sink which specifies the thermal radiation environment in which the radiator is placed. The temperature varies with the season (solar position), altitude, inclination, etc., but was found to be in the range of 220-280 K as a result of an orbital heat input analysis<sup>1</sup> carried out under the conditions of winter solstice/summer solstice, 250-460 km, 28.5 degrees, etc. Based on this result, heat exhaust capacity and weight estimation were carried out for a total of six cases by assuming 230, 250, and 270 K as the representative values for the heat sink temperature, and 300 and 310 K as the feeder temperature (maximum temperature on the panel surface) of the radiator.

Figure 1 shows graphs for the result of calculations carried out by taking the surface area of the single surface (not both surfaces) to be equal to the cargo bay door area  $22 \text{ m}^2$ , with the number of feeder lines as the parameter. From the figure it can be seen that the weight/capacity ratio (kgr/kW) of the radiator takes on a minimum value (optimum design) for the feeder line number of about 100. In this case, the heat exhaust capacity is about 7 kW, and the weight is about 110 kgr.

The cargo bay door of the HOPE is a curved rectangle plate  $3.0 \text{ m}$  wide and  $7.3 \text{ m}$  long. If  $1.2 \text{ m}$  of the  $1.5 \text{ m}$  long heat-pipe is used as a feeder, the figure shows  $7.3/1.2 \approx 6$ , so the feeder layout of this radiator consists of six segments as shown in Figure 2. Since the optimum number of feeders is about 100, and  $100/6 \approx 17$  and  $17 \times 6 = 102$ , the number of feeders to be installed is a total of 102. In this case, the half interval of the feeder installation is  $22 \text{ m}^2 / (2 \times 192 \times 1.2 \text{ m}) = 0.090 \text{ m}$ , so the width of the radiator is  $2 \times (102/6) \times 0.090 \text{ m} \approx 3.1 \text{ m}$ , the length is  $6 \times 1.2 \text{ m} = 7.2 \text{ m}$ , and the area is  $3.1 \times 7.2 \text{ m} \approx 22 \text{ m}^2$ , obtaining nearly equal shape/size to the cargo bay. This indicates that the result of the heat design is feasible from the equipment point of view.

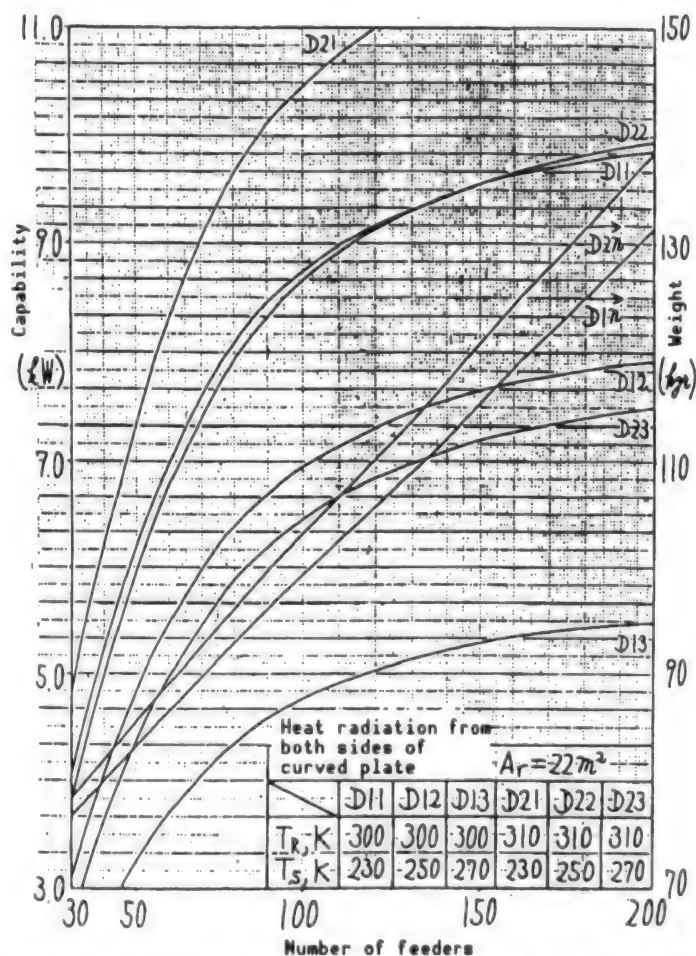


Figure 1. Heat Radiation Capability and Panel Weight

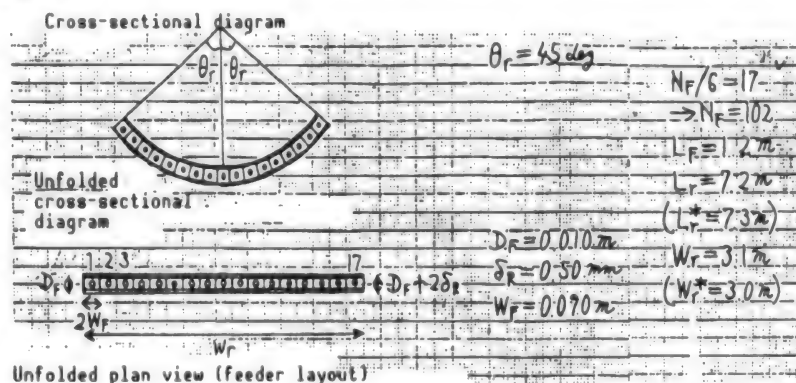


Figure 2. Radiator for HOPE



### 3. Structural Design Analysis

#### 3.1 Mechanical Environmental Conditions and Rigidity Requirements

In the design for HOPE as of the end of 1991,<sup>2</sup> the width of the carbo bay door was set to be 3.0 m in order to achieve 1) the reference weight, 2) the lateral natural frequency of 4 Hz when the radiator is rigidly fixed to the aircraft body, and 3) the longitudinal natural frequency of 20 Hz under the same condition. The launch environment of ETS-VI by H-II<sup>3</sup> is such that the maximum pseudo static acceleration is 3.2 g in longitudinal direction and 1.0 g in the lateral direction at liftoff, 6.0 g in the longitudinal direction and 1.0 g in the lateral direction at MECO. The resonance frequency in the longitudinal direction is 40, 65, 80 Hz, ..., and 25-28 Hz, 37-42 Hz in the longitudinal [as published]. In the launch of HOPE, the rocket is an H-II spinoff type (with six solid boosters) and the weight of HOPE is far greater than that of ETS-VI, so the launch environment is considerably different from what is given in the above. In order to sufficiently separate the natural frequency of the radiator from that of HOPE, minimum natural frequency of 30 Hz is set as a rigidity requirement. Since in the radiator for HOPE proposed in the previous section (Figure 2), a part (about 0.10 m each) of the left and right pieces overlap with each other at the time of unfolding, we chose the analytical boundary condition to be that of perfectly fixed on one end (the other end free).

#### 3.2 Estimation of Resonance Frequency

The radiator has the structure in which a fluid header and heatpipe feeders are installed on an aluminum sandwich panel. The panel rigidity strengthening effect of the header and the feeders is 14.1 percent for the longitudinal direction ( $L_r$ ) and 4.7 percent for the width direction ( $W_r$ ) which correspond to increases of 6.8 and 2.3 percent, respectively, in terms of natural frequency. That the radiator has a curved plate form helps to strengthen the rigidity in the longitudinal direction to some extent, but it does not contribute to the strengthening in the lateral direction. However, if it is assumed that the effective width (chord length of the circular cross section) is smaller than the unfolded width (circumferential length of the circular cross section) by 10 percent as shown in Figure 3, the first natural frequency will be improved by 17 percent. Accordingly, the natural frequency of this radiator can be estimated as the 20 percent augmented value of the natural frequency computed by assuming that it is a uniform rectangular plate. When the first natural frequency  $f$  of a uniform solid plate is determined according to the formula of Blevins<sup>4</sup>, p. 254 by taking the width  $a$  ( $W_r$ ) of the rectangle 3.1 m and the length  $b$  ( $L_r$ ) 7.2 m, the equivalent thickness has a uniform solid rectangular plate of the thickness of the aluminum sandwich panel, 6.92 mm, the surface density  $\gamma$  of the panel calculated from Figure 1, 4.3 kgr/m<sup>2</sup>, its Young's modulus,  $E$   $7 \times 10^{10}$  N/m<sup>2</sup>, the Poisson ratio,  $\nu$  0.3, and the condition defining factor,  $\lambda^2$  corresponding to the perfect one end fixing with  $a/b = 0.43$ , it is found to be 1.29 Hz. Therefore, its 20 percent augmented value  $f'$  is 1.55 Hz.



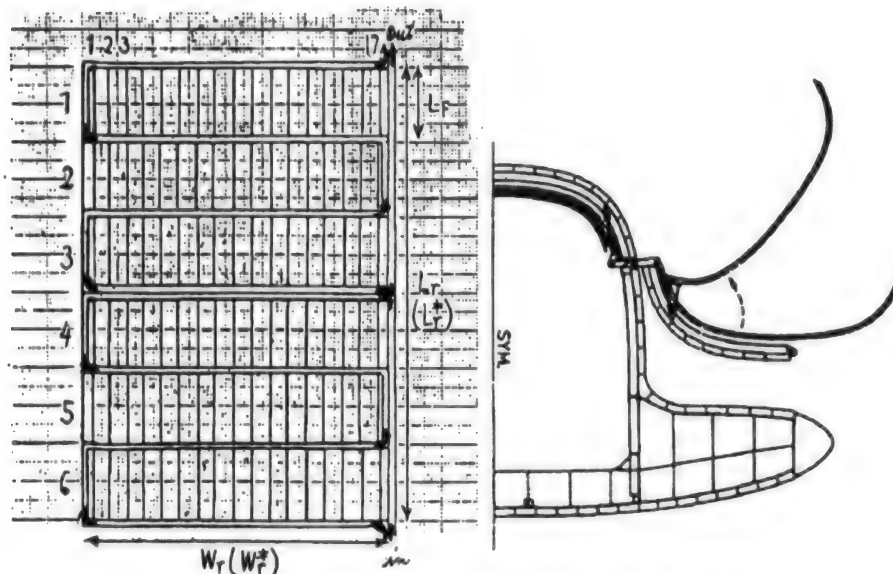


Figure 3. Airframe Cross Section of HOPE

### 3.3 Examination of Countermeasure and Necessity of Detailed Analysis

Since the above-mentioned value of  $f'$  does not satisfy the rigidity requirement, it is necessary to set up the new boundary conditions. If the entire circumference of the panel is fixed, the natural frequency becomes 6.7 times high which is about 19 Hz. The requirement of 30 Hz will be realizable in a panel of system of this structure by exclusively requiring to provide hold-down points (support with latches) at an interval less than 1 m. However, such a mechanism is not desirable for the situation in which a part of the left and right pieces overlap at the time of unfolding of the radiator.

Although it is possible to increase the rigidity by making the panel thick, this countermeasure brings about an increase of the total weight. It should be remembered that this analysis was performed based on a simple theoretical expression under the boundary condition of perfect fixing on one end, so it should move in the future to an analysis by finite element method (FEM). In addition, a header design (especially the pipe thickness setting) that pays attention to the damage of the fluid head due to collision of space dust will become necessary.

### 4. Conclusion

The radiator for HOPE proposed in this article nearly satisfies the thermal requirements, but structurally speaking, the rigidity is not sufficient, so weight increase to some extent for strengthening the rigidity is inevitable. In the future it will further be necessary to set structural requirements, and to specify the boundary conditions, especially the hold-down points.

### References

1. Furukawa, M., "Equivalent Sink Temperatures and Space Radiator Design Practices," Proceedings of 18th ISTS, Kagosima, Japan, May 1992, e-1-1.
2. H-II Orbiting Plane HOPE Conceptual Design Report, Executive Summary on the Design Status, December 1991, NASDA (English version).
3. Nakano, T., Tomioka, K., and Ujino, T., "Flight Dynamic Environment of H-II Launch Vehicle," Proceedings of 17th ISTS, Tokyo, Japan, May 1990.
4. Blevins, R.D., "Formulas for Natural Frequency and Model Shape," Van Nostrand Reinhold Co., 1978.

## **Structural Materials for HOPE Reentry Vehicle**

936C1015G Tokyo KOZO KYODO NI KANSURU KOENKAI in Japanese 15 Jul 92 pp 210-213

[Article by Yoshiki Morino, Toshinari Yoshinaka, Hirobumi Tamura, and Yoichi Sato, National Space Development Agency]

[Text] **Abstract:** The research status of structural materials for the HOPE reentry vehicle is presented and technical considerations are discussed.

### **1. Introduction**

As a part of the research and development<sup>1</sup> on the H-II rocket launch type winged recoverable airplane (HOPE) planned by NASDA, we have been examining the materials for the main structures of HOPE and the carbon/carbon (C/C) materials to be applied to ultrahigh-temperature sites. In this article we will give a brief report on the result of investigation of the basic tests relating to these heat-resistant structural materials and the problems in the future.

### **2. Summary of Structures and Materials Application Plan**

The plan is for HOPE to be launched attached to the tip of the H-II rocket (or a rocket derived from it), orbit, reenter the atmosphere, and land horizontally on the runway. The most significant feature regarding the body structure is that it has relatively large tip fins at the tips of the main wing from the requirement of aerodynamic performance, and that the tip fins are exposed to a severe aerodynamic heating environment at the time of reentry. According to the examination of the conceptual design so far, we are investigating the use of C/C materials for the tip fin structure due to its heat resistance and outfitting, and the application of C/C materials to various kinds of rudder surface structures, though there still remain technical problems concerning aerodynamic heating estimates. In the development of hot structures from C/C materials it is necessary to develop coating technology to secure heat resistance and to examine and develop structural format that takes into account the characteristics of the C/C materials. The front end part of the fuselage and the front edge part of the main wing will be given monocoque structure similar to that of the U.S. space shuttle, where heat resistance at the 1,700°C level will be required of the C/C material.

Other structural features are that the fuselage has at its central part a large indentation, that the load at the rear half of the fuselage is large because it is to be launched placed at the tip of the rocket, that it is necessary to secure access to the equipment, etc., in the front and rear halves of the fuselage. In addition, the load is relatively large even at the wing tip part since the tip fins are attached there as mentioned earlier.

Besides these requirements for structural strength, it is necessary to consider "development of lightweight structures that can withstand the aerodynamic heating environment, can suppress the infiltration of heat into the body, and takes into account the in and out flows of heat while it is in orbit," as the requirements analogous to other similar airplanes.

For the main structures of the main wing and fuselage of HOPE, based on a comparative examination of the total weight of the main structures, the thermal protection system (TPS), and the heat insulation materials on board, carbon polyimide (C/Pi, fiber is T800H and resin is PMR-15) which is expected to result in large weight reduction compared with other materials such as aluminum alloys, was selected as the primary candidate material, and an examination of the structural design and acquisition of basic data are in progress.

### 3. Basic Tests on Carbon Polyimide Composite

In applying C/Pi which is under examination as the main structural material for HOPE, the main technical problems are the evaluation of its impact on the characteristics of thermal cracks and the establishment of the forming technology. Thermal cracks generated by the aerodynamic heating environment and the heat cycles in the orbit have little effect at normal temperature.<sup>2</sup> Regarding the forming technology, there are problems to be solved in developing the actual body structure, such as the high temperature at molding, gas generation at the time of hardening, and tucking property of preregs.

#### (1) Thermal Cracks

The property evaluations under the worst environment regarding the operating conditions of HOPE include the degree of effect of thermal cracks, that are generated through 10 planned operations, on the compressive strength and on the compression after impact (CAI) strength, which determines the limit compressive strain, at the time of high temperature and moisture (HOT/WET). A summary of the result of the tests carried out on a unidirectional pseudo-uniform laminate concerning the effect of thermal cracks on the HOT/WET compressive strength and the temperature dependence of the HOT/WET strength is shown in Figure 1. Here, the heat cycles are taken

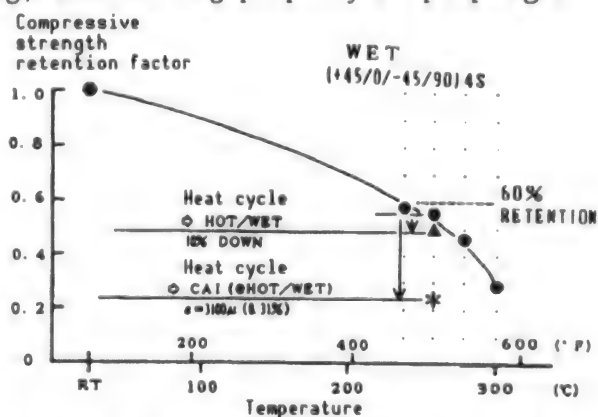


Figure 1. Compressive Strength Retention Factor of C/Pi in HOT/WET Condition

into consideration, in which the temperature rise due to the aerodynamic heating at launch and reentry and changes from sunshine to sunshade that occur in orbit. In the CAI test, emphasis was placed on understanding the extent of influence of the heat cycles. An impact was given after exposure to heat cycles corresponding to five flights, and the HOT/WET compressive strength test was given after further exposure to heat cycles corresponding to one flight. The test result may be evaluated roughly as follows.

- 1) The reduction rate of the HOT/WET compressive strength after giving heat cycles is minimally about 10 percent, so it is not necessary to consider a large reduction of the strength due to synergetic effect of the thermal cracks and the HOT/WET environment.
- 2) The CAI distortion under the combined heat cycles and HOT/WET environment maintained the value of  $3,100 \mu$ , showing that it has characteristics comparable even to epoxy composite materials that are not subjected to heat cycles, and has an excellent characteristic even under the combined condition of these two factors.
- 3) In addition, there is little significant difference between the damaged area after impact and the damaged area after exposure to an additional heat cycle which corresponds to one flight, so the heat cycles pose little effect on the damaged area.
- 4) Furthermore, regarding the temperature dependence of the HOT/WET compressive strength, the applicable maximum temperature for the "strength holding rate of 60 percent," for which there are many application examples of epoxy composites, is  $260^{\circ}\text{C}$ , so it is desirable to set the upper limit of the operating temperature at about  $260^{\circ}\text{C}$ .

## (2) Forming Test

Following the trial manufacture of components of 1 meter in size such as reinforcing skin and curved surface frames,<sup>3</sup> small components 1 meter in size that are closer to actual structures, with the inter-spar structure of the main wing as the model, were trial manufactured. The following is a summary of 1) the result of the test on a thick reinforcing skin with stringers of variable thickness for the doubler, and 2) the result of the test on integrally molded spar/skin structure.

Figure 2 shows the appearance of a specimen of thick plate reinforcing skin with double reinforcement. The UD material is used with specimen length in the stringer longitudinal direction of 1 m, and lamination number of 36 plies (4.8 mm) in the general part and 56 plies (7.5 mm) in the doubler part. The result of the quality test by ultrasonic flaw detection and cross-section observation was satisfactory, and it was confirmed that an integral molding of a thick plate and a reinforcing skin with variable thickness is possible.



Figure 2. Trial Manufactured Skin With C/Pi Thick Plate

In Figure 3 is shown the appearance of a trial-manufactured integrally molded specimen of spar. The specimen has a length of 1 m and spar height 200 mm, and the number of laminations is 12 ply (1.6 mm) in the skin and 26 ply (3.5 mm) in the spar cap part where use is made of UD material, and taper is given by imagining that the mold lines of the main wing skin run in the cord direction (direction perpendicular to the spars). The result of the test on the specimen was generally satisfactory, and an integral molding was thought to be possible for structures that have three-dimensional shape of the level of spar/skin structure, although restrictions on the complexity or the like of other shape, board thickness, etc., are conceivable.

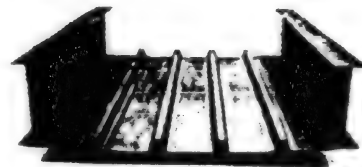


Figure 3. Trial Product of Integrally Manufactured C/Pi Spar Skin

As in the above, a sufficiently detailed evaluation was carried out for the principal material characteristics that consider the operating environment of HOPE, and a satisfactory result from the viewpoint of the molding technology that imagines the structures for the actual airplane was obtained. In applying C/Pi to the main structures of HOPE, solidification of data on characteristics and setting of design tolerance values, and examination of the molding technology for enlargement of structures corresponding to the actual aircraft and complicated structures have to be performed further, to establish the technologies and to set the jig structures and the molding processes.

#### 4. Basic Tests on Carbon/Carbon Composites

The C/C composites are indispensable materials in the development of HOPE, and, along with the development of the oxidation resistant technology that secures heat resistance, development and evaluation as structural materials are important technical problems in applying these materials to structures between tip fin spars which are required to have load transfer capacity. Here, the result of examination of the materials as structural materials will be presented.

##### (1) Mechanical Characteristics

The level of the mechanical characteristics of a plurality of C/C materials being examined as heat-resistant materials for HOPE are shown in Figure 4. Although the in-plane strength is at high level of 20-30 kgf/mm<sup>2</sup> compared with RCC used for the space shuttle, the interlayer shearing strength is at a low level of 1-2 kgf/mm<sup>2</sup>. The fracture strain is at low level of 1,000-3,000  $\mu$ , so it is necessary to give a sufficiently detailed study such as the consideration in design for examination of feasibility of the C/C composites.

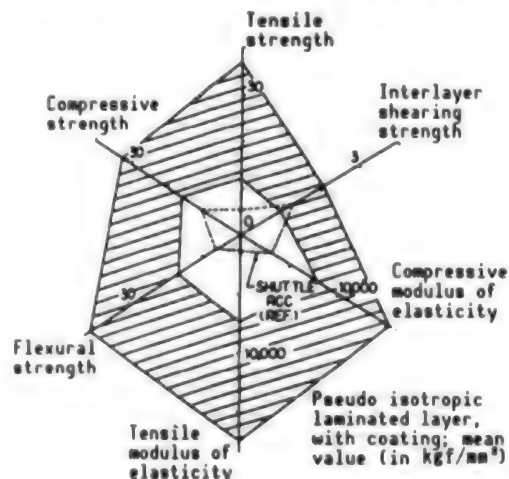


Figure 4. Mechanical Properties of C/C Material



## (2) Bending Strength

Since there is a possibility of having the problem of interlayer fracture at the corner parts of spar cross section, etc., bending strength test was carried out for the purpose of understanding the load transfer capacity. The result is shown in Figure 5. The fracture mode is that of interlayer fracture, and it can be estimated that it has the load resistant capacity of about 100 kgf.

In the application of C/C composites to the tip fin structures, it is necessary to have sufficiently detailed examination by tests on trial manufactured products such as the development of the structural format that considers the characteristics of the C/C materials, understanding of the fracture mode and the load resistance capacity, the development and evaluation of the fastener and joint structures, the establishment of the molding technology on the component level, etc.

## 5. Conclusion

The development of heat-resistant materials and their structure technology are technical problems that occupy an important position in the development of HOPE, and requires a wide range of investigation including the development evaluation of materials, design, techniques and facilities of evaluation tests, etc. We ask the cooperation of various organizations to be continued in the future.

## References

1. Eguchi, A., et al., "The Status of the HOPE Concept Study," 18th ISTS, Kagoshia, 1992.
2. Morino, Y., et al., "R&D on HOPE Structure," Ibid.
3. Matsushita, T., et al., "Research on Heat-Resistant Main Structural Members for HOPE (Carbon/Polyimide)," Collected papers for 32nd Meeting on Structural Strength, July 1990.
4. Morino, Y., et al., "Research and Development on Heat-Resistant Materials for HOPE," Collected papers for 33rd Meeting on Structural Strength, July 1991.

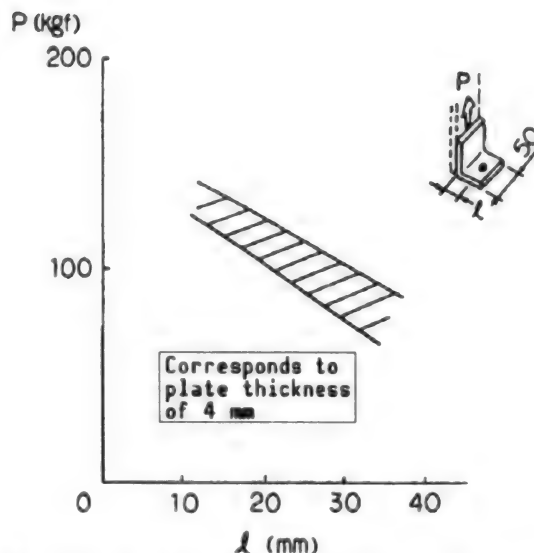


Figure 5. Bending Strength of C/C Material

## **POGO Analysis of H-II Rocket Ground Firing Test**

936C1015H Tokyo KOZO KYODO NI KANSURU KOENKAI in Japanese 15 Jul 92 pp 214-217

[Article by Takumi Ujino, NASDA, and Yujiro Shirai and Mayuki Nitsu, Mitsubishi Heavy Industries, Ltd.]

[Text] **Abstract:** Vibration tests of the aircraft body and a propulsion system dynamic characteristics test were carried out to evaluate the unstable vibration phenomenon (POGO) in the ground firing test of the H-II rocket, and POGO analysis was carried out based on the test results. According to the analysis, it was found that POGO does not occur in the ground firing test. In the actual ground firing test, vibration phenomenon caused by POGO did not take place either, showing the validity of the POGO characteristics evaluation techniques.

### **1. Introduction**

Preventing the generation of POGO which is a compound unstable vibration of the structural system and the propulsion system is the key for the development of liquid fuel rockets. In the H-II rocket, preventing POGO generation has been continued since the initial stage of the development of the rocket<sup>1</sup> and a dedicated POGO suppression device called PSD was developed.<sup>2</sup> However, it is possible that POGO is generated not only during flight but also in the ground firing test, and examples of its generation have been reported in the development of the space shuttle. In this report, the POGO characteristics evaluation techniques in the first stage ground firing test (BFT-1), namely, the body vibration test, the propulsion system dynamic characteristics test, and POGO analysis, and the result of the ground firing test will be discussed.

### **2. POGO Characteristics Evaluation Techniques**

A POGO characteristics evaluation in the ground firing test was carried out according to the flow shown in Figure 1. Since POGO is a compound unstable vibration phenomenon of the structural system and the propulsion system, it is necessary for POGO characteristics evaluation to acquire both body vibration characteristics and propulsion system dynamic characteristics. Using the acquired data an analytical model was constructed, analysis was done for the ground firing test by analytical techniques similar to the POGO analysis during flight (Figure 2).

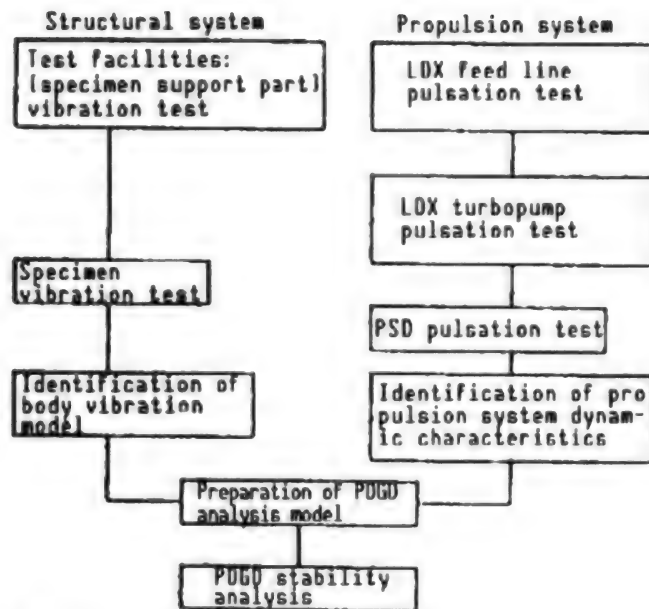
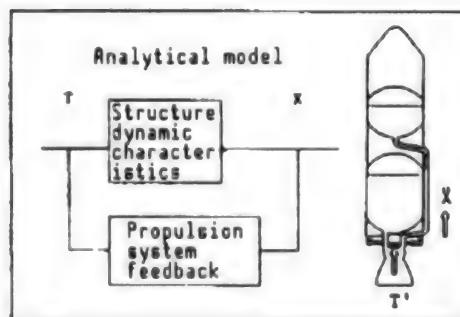


Figure 1. POGO Characteristics Evaluation Techniques



#### Evaluation Index

$GM > 0$  Unstable,  $GM$  : Gain margin  
 $GM < 0$  Stable

where

$$GM = 20 \text{ LOG } (\zeta_N / \zeta_S)$$

$\zeta_N$  : Modal attenuation of structure

$\zeta_S$  : Structural attenuation required for stability of system (approximate value at POGO generation frequency  $\omega_0$ )

$$\zeta_N = -G_e / H \text{ I} / 2, G_e \text{ is structure gain}$$

$H \text{ I}$  is the imaginary part of  $H(\omega_0)$

Figure 2. POGO Stability Analysis Techniques

### 3. Result of the Test

#### (1) Vibration Test

Since in the ground firing test, differing from the case in flight, the specimen is supported by the ground test facility, tests were given for the specimen supporting part of the testing facility and for the specimen in the state of being supported, and the natural frequency characteristic was obtained. A schematic diagram of the test is given in Figure 3, and the acquired natural frequency characteristic is shown in Table 1 and Figure 4. The specimen vibration test was carried out in the empty fuel configuration. The first order vibration mode of the specimen is the rigid body mode of the specimen (the supporting part mode), the second order mode is the longitudinal fundamental mode of the specimen, and the third order mode is the cross beam mode where the engines are fixed. These vibration modes were used for the examination of the POGO characteristics.

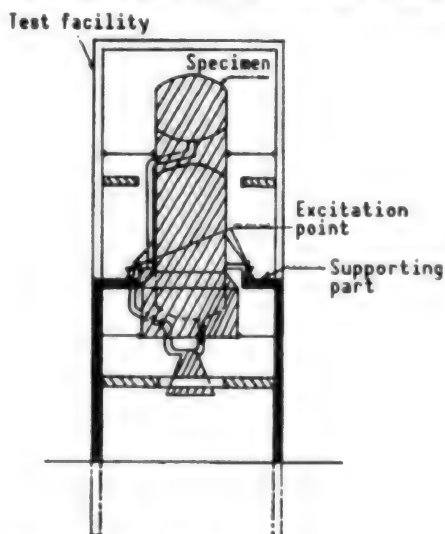


Figure 3. Method of Body Vibration Test

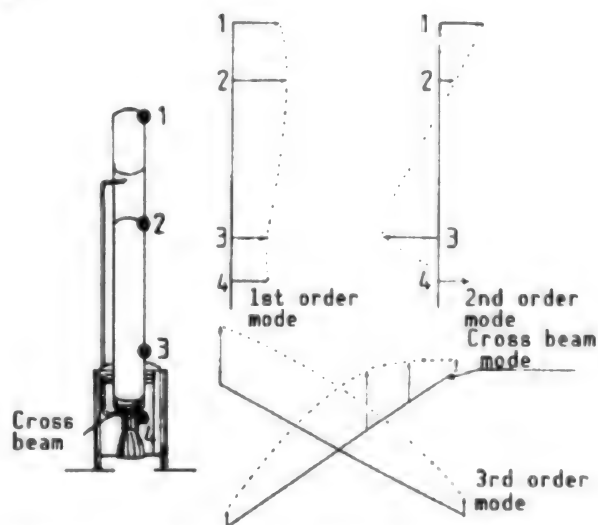


Figure 4. System of Body Vibration Modes (Vertical direction of body)

Table 1. Natural Frequency Characteristic of Aircraft Body

Test form	Vibrational mode	Natural frequency
Specimen	1st order mode	14.6
Specimen	2nd order mode	48.7
Specimen	3rd order mode	58.1

#### (2) Propulsion System Dynamic Characteristics Test

From the examinations in the past it is known that the dynamic characteristics of the LOX system in the propulsion system is dominant. For this reason,

pulsation tests for acquiring the propulsion system dynamic characteristics were carried out for the LOX feed line, PSD, and the turbopump. A summary of each test is given in Table 2. For PSD in particular the compliance and resistance are so arranged to be adjustable for suppressing POGO (Figure 5), and for that reason it is particularly important to acquire characteristics in advance. The acquired PSD characteristics are shown in Figure 6. Further, particularly high precision is required for the turbopump dynamic characteristics since the turbopump dynamic characteristics greatly influence the POGO characteristics.

**Table 2. Details of Propulsion System Pulsation Test**

Test item	Detail of test	Acquired characteristics
LOX feed line pulsation test	To acquire pressure distribution of LOX feed line by applying pressure pulsation to one end of the LOX feed line	Pressure transfer characteristic
PSD pulsation test	To acquire PSD internal pressure by applying pressure pulsation to the PSD inlet	Compliance resistance
Turbopump pulsation test	To acquire pressure variation and flow rate variation by applying pressure pulsation at the time of turbopump characteristic test	Cavitation compliance, mass flow gain factor

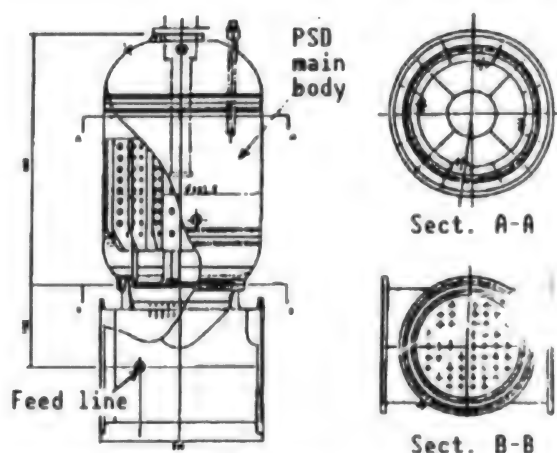


**Figure 5. POGO Suppression Mode**

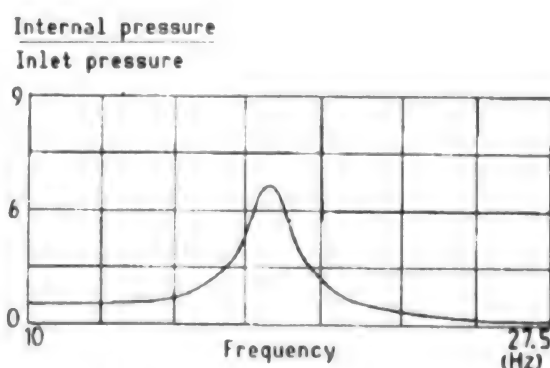


**Figure 6. PSD Characteristic Curve**

#### 4. Result of Analysis

A stability analysis of the ground firing test was performed by identifying the POGO analysis model based on the result of the body vibration test and the propulsion system dynamic characteristics test. The overall analysis model is shown in Figure 7, and the change with the firing time in the natural frequency of the body and the natural frequency of the propulsion system are shown in Figure 8. Since the natural frequency of the body changes markedly according to the fuel consumption, the analysis was carried out in Figure 8 at every time of firing. Since the body vibration test was carried out in the state of empty fuel, the vibration model for other fuel conditions was determined by analysis based on the model for empty fuel state.

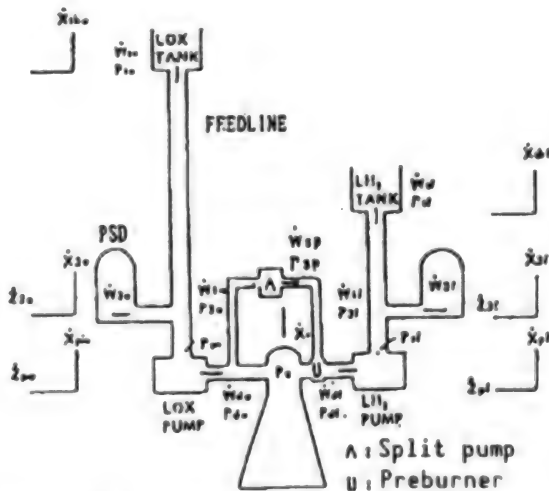


Figure 7. POGO Stability Analysis Model

Further, since the thickness of the tank is large, fuel was treated as an additive mass. The result of the stability analysis is shown in Figure 9. In Figure 9 the gain margin of the second order mode is about 20 dB, so it can be seen that unstable vibration phenomenon will not be generated. In addition, sensitivity analysis was carried out for the dynamic characteristics of the LOX turbopump which affect strongly the POGO characteristics, the cavitation compliance, and the mass flow gain factor (Figure 10). For the variation range of the imagined pump dynamic characteristics, it was anticipated that no POGO will be generated. Based on this result, we moved to the actual firing test, but no POGO generation was observed. A representative measurement result is shown in Figure 11. In Figure 11 nothing other than random vibrations accompanying firing is measured, showing that the analysis is correctly estimating the firing test result concerning POGO generation and that the POGO characteristics evaluation techniques is valid.

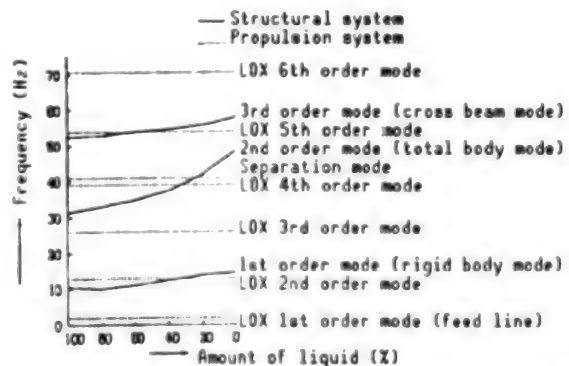


Figure 8. Result of Natural Frequency Analysis

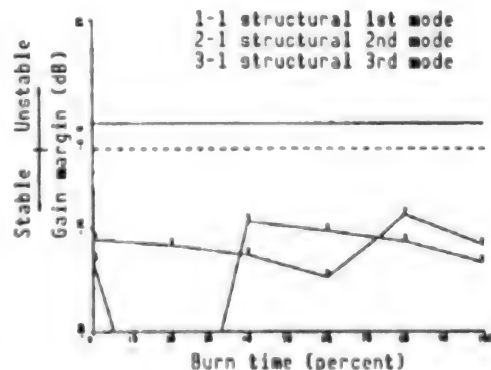


Figure 9. Result of Stability Analysis



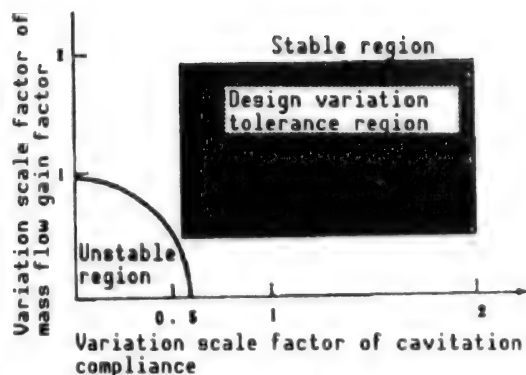


Figure 10. Result of Sensitivity Analysis of LOX Turbopump Characteristic

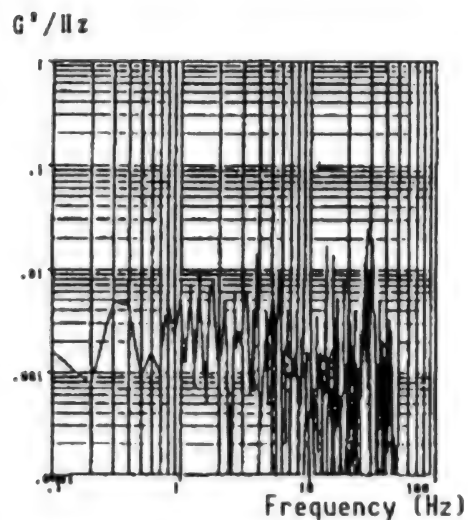


Figure 11. Result of Ground Firing Test (Vertical acceleration of the thrust mount)

## 5. Conclusion

In liquid fuel rockets, POGO suppression is an important problem. In the future we are planning to revise the analytical model for the structural system and the propulsion system through utilization of the result of the ground firing test and various kinds of tests in order to improve the evaluation accuracy of the POGO characteristics during flight.

## References

1. Morino, Y., Motio, T., Kosetu, Y., Mori, T., and Shirai, Y., "Preliminary POGO Stability Analysis of H-II Launch Vehicle First Stage," 15th ISTS, 1986.
2. Ujino, T., Morino, M., Kosetu, Y., Mori, T., and Shirai, Y., "POGO Analysis on the H-II Launch Vehicle," AIAA/ASME/ASCE/AHS 30th Structures, Structural Dynamics and Material Conference, 1989.

## Study on POGO Analysis of Liquid Launch Vehicle

936C10151 Tokyo KOZO KYODO NI KANSURU KOENKAI in Japanese 15 Jul 92 pp 218-221

[Article by Shigeo Kobayashi, Science University of Tokyo, and Ken Fukuda, Toyota]

[Text] **Abstract:** The POGO property of the H-II launch vehicle has been calculated. The results yield the following improvement on the method of analysis. The mass flow gain factor should be taken in the expression of the pump property. The modal pressure derived in the analysis of normal modes of vibration should be used as the value of tank bottom pressure.

### 1. Introduction

Since the first stage of the H-II rocket is a newly started development, its POGO analysis is being carried out by NASDA and other organizations.<sup>1,2</sup> When the analytical method used previously by the authors for the N rocket is applied to it, a result which differs from that of NASDA was obtained. In this article we will discuss the result of our investigation about the causes of the difference.

### 2. Theory of Analysis

When the longitudinal vibration  $u(x,t)$  of the rocket is expanded in terms of the normal vibration modes  $\phi_n(x)$  as

$$u(x,t) = \sum u_n \phi_n(x) \quad (1)$$

the equation for each coefficient  $u_n$  is given by the following equation:

$$M_n \left( \frac{d^2 u_n}{dt^2} + \eta \omega_n \frac{du_n}{dt} + \omega_n^2 u_n \right) = T \phi_n(0) + \sum_j^{F,0} [(-p_s^j A_I^j \phi_n^j(0) + \rho^j h^j \frac{dQ_R^j}{dt} + p_t^j A_I^j) \phi_n^j(t_b)] = M_n x H(i\omega) \frac{du_n}{dt}, \quad H(i\omega) = H_R + iH_I \quad (2)$$

The analytical model for the propulsion system is shown in Figure 1. The pressure variation at the tank bottom is expressed by

$$p_t = \rho h \left[ \left(1 - \frac{A_l}{A_t}\right) \phi_n(tb) \frac{d^2 u_n}{dt^2} - \frac{1}{A_t} \frac{dQ_t}{dt} \right] \quad (3)$$

The pressure variation and the flow rate variation at the feed pipe terminals (accumulator inlet and pump inlet) are given, respectively, by

$$p_s + \cos \omega \tau \cdot p_t - i(L_1/\tau) \sin \omega \tau \cdot Q_t \quad (4)$$

$$Q_s = -i(\tau/L_1) \sin \omega \tau \cdot p_t + \cos \omega \tau \cdot Q_t \quad (5)$$

$$\text{where } \tau = Q/c \text{ (c is the velocity of sound) and } L_1 = \rho Q/A^l \quad (6)$$

The characteristics of the accumulator (POGO suppression device (PSD)) are given by

$$Q_s = p_s / [i\omega L_s + R_s + \{K_s + (\rho n g / A_s)\} / (i\omega)] \quad (7)$$

$$K_s = \gamma P_{s0} / V_{s0}, \quad L_s = \rho H_s / A_s \quad (8)$$

The characteristics of the pump are given, with the mass flow gain factor  $C_{mg}$  and the cavitation compliance  $C_b$  by

$$p_d + (m_p + 1)p_s - (i\omega L_p + R_p)Q_d \quad (9)$$

$$Q_d = (1 - i\omega C_{mg})(Q_s + A_l(du_n/dt) - Q_s) - Q_b, \quad Q_b + i\omega C_b p_s \quad (10)$$

The discharge line characteristic is given by

$$p_c = p_d - (i\omega L_d + R_d)Q_d \quad (11)$$

The thrust chamber characteristics are given by

$$(1 + i\omega \tau_c)p_c = (C^* \rho^* Q_d^* + C^* \rho^* Q_d^*) / A_{th} \quad (12)$$

$$T = C_T A_{th} p_c \quad (13)$$

From these relations  $H_R$  in Equation (2) is calculated as

$$D_R(\omega_n) = H_R(\omega_R) / \omega_R - \eta \quad (14)$$

and it is judged unstable if its sign is positive.

### 3. Result of Calculations and Consideration

The calculated value for  $D_R$  of the characteristic vibrational mode of the single system of LOX up to the fifth order, with  $C_{mg} = 0$ , using numerical values (details omitted) borrowed from NASDA. The result for the cases of

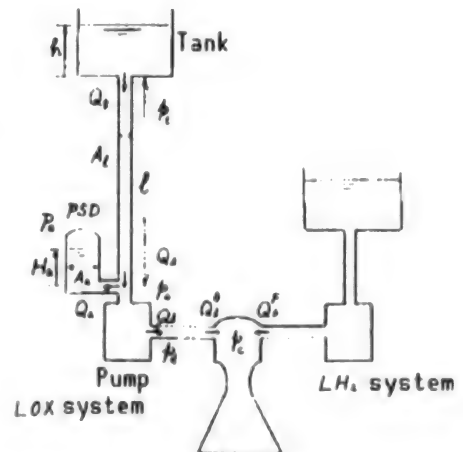


Figure 1. Analytical Model and Notations

PSD-off and PSD-on are shown in Figures 2 and 3, respectively. After separation of the solid booster the first order characteristic vibrational mode disappears. Figure 2 shows that the lowest order (second order) mode undergoes MECO POGO, and the other modes are stable. Figure 3 shows that the MECO POGO is completely suppressed by PSD-on. That the result of the calculation for the single  $\text{LH}_2$  system is stable is shown by the fact that the result of calculation for a combined system of LOX and  $\text{LH}_2$  does not differ much from the result of calculation shown in Figures 2 and 3. The result of calculation according to the simplified expression, Equation (41) of reference 3, is similar to that in Figure 3 for the case of PSD-off, but differs from that in Figure 3 for the case of PSD-on because the terms including  $L_a$  and  $R_a$  in Equation (7) are omitted there, but is stable over the entire range and does not affect the stability.

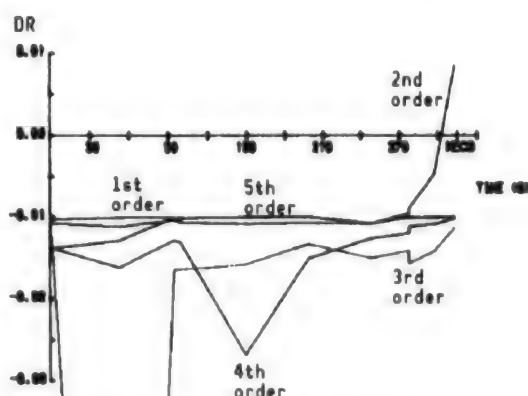


Figure 2. LOX Single System  
( $C_{mg} = 0$ ), PSD-OFF

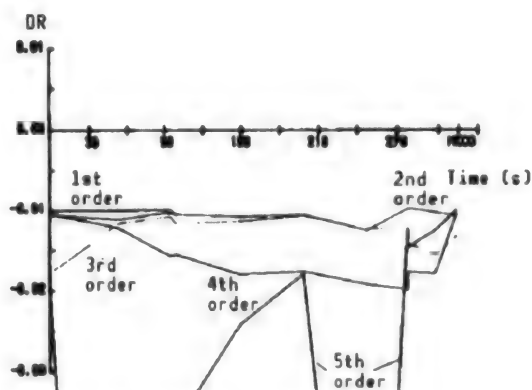


Figure 3. LOX Single System  
( $C_{mg} = 0$ ), PSD-ON

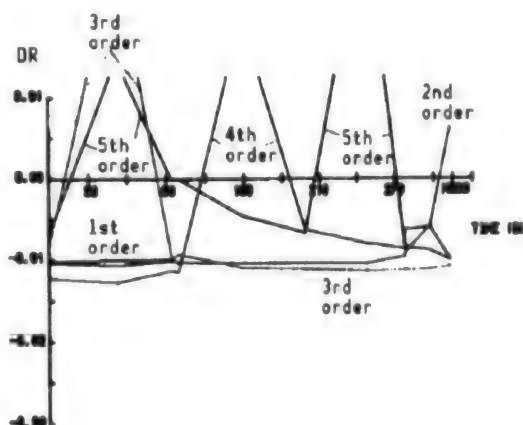


Figure 4. LOX Single System  
( $C_{mg} = 0.003$ ), PSD-OFF

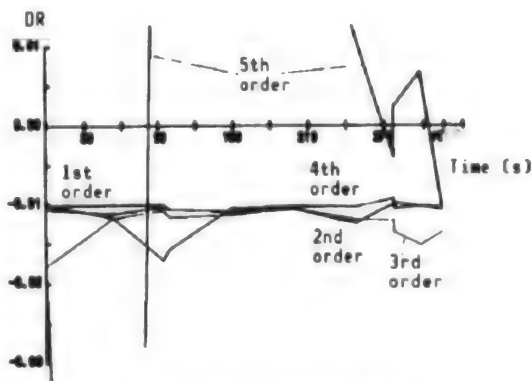


Figure 5. LOX Single System  
( $C_{mg} = 0.003$ ), PSD-ON

The results of calculation for the cases of  $C_{mg} = 0.003$  (standard value) and 0.001 are shown in Figures 4~7. For the case of  $C_{mg} = 0.003$ , Figure 4 shows that there appear unstable regions due to the third, fourth, and fifth order modes for PSD-off, and Figure 5 shows that the instability due to the fifth

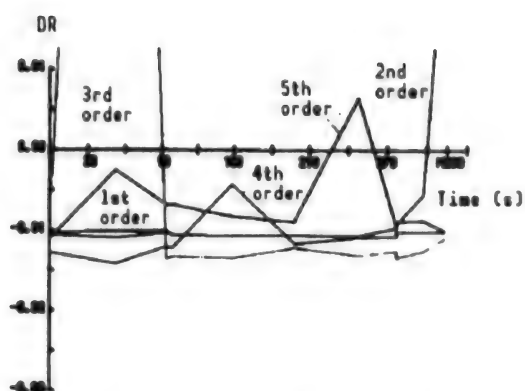


Figure 6. LOX Single System  
( $C_{mg} = 0.001$ ), PSD-OFF

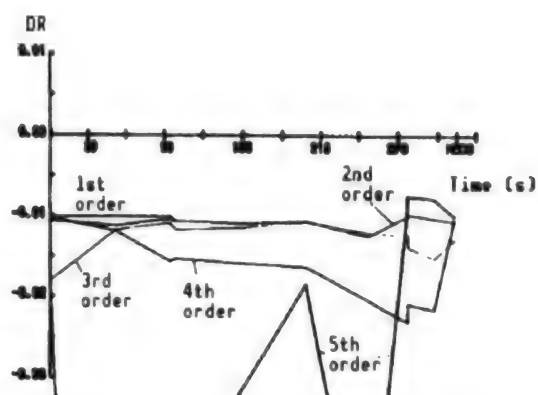


Figure 7. LOX Single System  
( $C_{mg} = 0.001$ ), PSD-ON

order mode cannot be removed even in the PSD-on state. When the value for  $C_{mg}$  is reduced to 0.001, Figure 6 shows that instability arises for the third and fifth order modes, but Figure 7 shows that all the modes become stable in the PSD-on state, so it can be concluded that the value of  $C_{mg}$  has an important meaning. Figure 8 shows that even for  $C_{mg} = 0.003$  stability can be obtained for PSD-on by setting the value of  $L_p$  of PSD to one-third of the standard value  $1.47 \times 10^4 \text{ kg/m}^4$ .

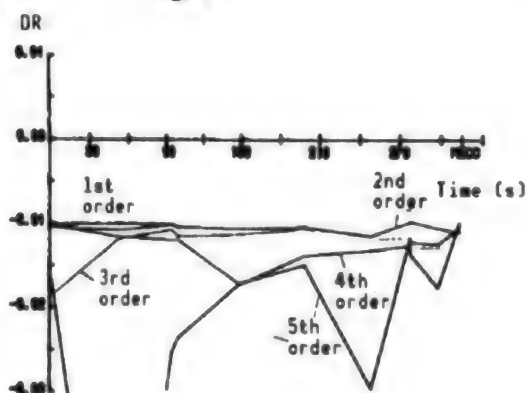


Figure 8. Total System ( $C_{mg}^0 = 0.003$ ,  $C_{mg}^F = 0.005$ ,  $L_p/3$ ), PSD-ON

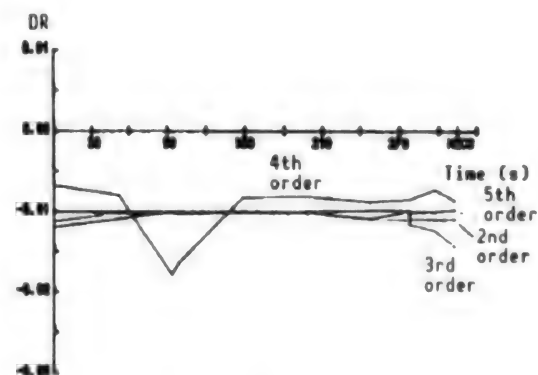


Figure 10. Total System  
( $C_{mg}$ : standard value,  $p_t$ : modal analysis value), PSD-ON

However, according to the result of calculations by NASDA, the instability for PSD-off for  $C_{mg} = 0.003$  occurs only in the second, third, and fourth order modes alone, and stability can be achieved by PSD-on, showing no instability involving the fifth order mode. An investigation on the cause of the difference revealed that the calculations by NASDA uses as the value for  $p_t$  at the tank bottom, not Equation (3) above, but the value for  $p_t$  in each vibrational mode evaluated in the characteristic vibration analysis which takes into account the deformation of tank bottom and the motion of the fluid due to BEM/FEM.<sup>4,5</sup> The result of the N rocket test was nearly satisfactory by using a specific vibrational mode under the assumption that the tank bottom, 2.4 m in diameter, undergoes an identical displacement as the outer cylinder.

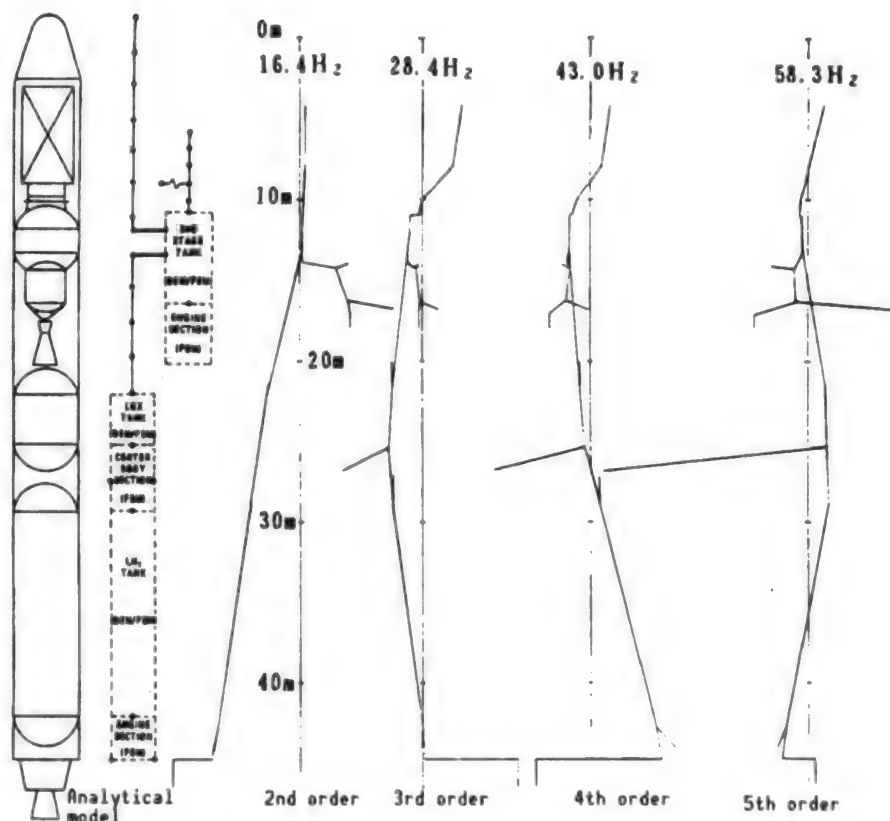


Figure 9. H-II Rocket Longitudinal Vibration Modes (2nd to 5th orders)

However, in the H-II rocket the characteristic vibrational modes of the up-down motion of the outer cylinder and its interior have different forms as shown in Figure 9 because of the thin tank bottom structure and the flexible engine supporting cross beams. It was found that  $p_t$  by the characteristic vibration analysis and  $p_t$  calculated from the characteristic vibrational mode  $u_n$  differ considerably. It was found that the result of calculation using the modal pressure  $p_t$  of NASDA instead of Equation (3) shows stability over the entire range for PSD-on as shown in Figure 10.

#### 4. Conclusion

- 1) Recently, it became possible to estimate the value of  $C_{mg}$  of the pump, but it is important to consider the effect of  $C_{mg}$  in the POGO analysis of H-II.
- 2) A light structure with a large diameter such as the H-II rocket cannot simply adapt longitudinal vibrations of a one-dimensional rod. It is necessary to use the tank bottom pressure  $p_t$  obtained by the specific vibrational mode analysis in the POGO analysis.
- 3) It can be considered that the result of POGO analysis by NASDA is valid if  $u_n$  and  $p_{tn}$  of characteristic vibration analysis are correct ones.



The authors are grateful to Dr. Yoshiki Morino, NASDA, who kindly made the data and the result of analyses on POGO of H-II rocket available to them.

#### References

1. Ujino, T., et al., "POGO Analysis on H-II Launch Vehicle," AIAA SDM, April 1989.
2. Ujino, Ishii, and Kaneno, "A Method of POGO Stability Analysis of Liquid Launch Rocket and Its Applications to H-II Rocket," Collected papers for 31st Meeting on Structural Strength, July 1989, p 388.
3. Kobayashi and Kojima, "Self-Excited Longitudinal Vibration (POGO) of Liquid Launch Rocket," J. OF JAPAN AEROSPACE SOCIETY, June 1987, p 354.
4. Morino, Y., et al., "Vibration Test of One-Fifth Scale H-II Launch Vehicle," AIAA SDM-87-0783, April 1987, p 242.
5. Morino, Kosetsu, and Asada, "Vibration Characteristics Analysis of H-II Rocket," Collected papers for 29th Meeting on Structural Strength, July 1987, p 58.

## **Tensile Properties of Inconel-718 With Welded Joint**

936C1015J Tokyo KOZO KYODO NI KANSURU KOENKAI in Japanese 15 Jul 92 pp 266-269

[Article by Tomoyuki Hashimoto and Yoshiaki Watanabe, National Aerospace Laboratory, and Mitsumasa Sakamoto, Mitsubishi Heavy Industries, Ltd.]

[Text] **Abstract:** The LE-7 engine that will be used as the H-II rocket main engine has been developed by Japan. This engine has a lot of welded joints, and various troubles have occurred at those joints. So, tensile properties of Inconel-718 testpieces with a welded joint were investigated at various temperatures in high pressure hydrogen and helium gas. It was found for the welded joint that the limpness at the welded part led to decreased ductility and that the massed shape of intergranular  $\text{Ni}_3\text{Nb}$  led to decreased tensile resistance.

### **1. Introduction**

Currently, development is under way in this country on LE-7 to be used as the first stage engine of the H-II rocket. In the manufacture and assembly of LE-7 many welded joints are used, and numerous nonconformities are found in the welded joint parts in the process of the development. Because of this, specimens for tensile test of Inconel-718 welded joint were manufactured to give them tensile test in He and  $\text{H}_2$  atmosphere, and the mechanical strength and sensitivity to hydrogen embrittlement of welded joints at normal and high temperatures was studied. In addition, based on the result, the relationship between the mechanical strength and the microstructure is discussed.

### **2. Method of Test**

TIG and EBW welded joint test specimens were manufactured, and to compare the tensile strength, another testpiece of the base material was manufactured. The joints were processed in the shape appropriate for testing after welding. The heat treatment included solution annealing at 1,227 K for 1 hour, two-stage aging test at 993 K for 8 hours, and 893 K for 10 hours. The specimen dimensions are given in Figure 1.

Tests were given at room temperature, 500 K, 700 K, 900 K, and 1,000 K in the test atmosphere of He and  $\text{H}_2$  at 19.7 MPa. The tensile test was given until fracture at the head speed 0.3 mm/min of the tensile testing machine.

Measurements included the tensile strength, 0.2 percent bearing force, elongation at the gauge length 35 mm, and contraction of area. In addition, fractography examination and cross section inspection were performed using scanning electron microscope (SEM) and optical micrograph.

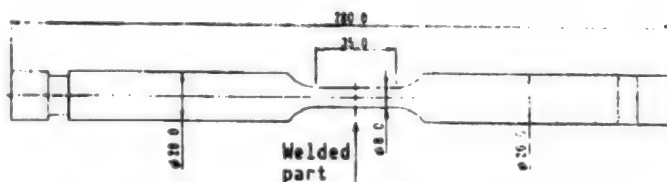


Figure 1. Shape of Tensile Testpiece

### 3. Result of Test

Figure 2(a) shows mechanical properties of TIG welded joint in He and H<sub>2</sub> atmosphere at various temperatures. The TIG welded joint is inferior to the base material in all of the 0.2 percent yield strength, tensile strength, elongation, and contraction of area. Rupture occurred always with its face approximately perpendicular to the axial direction in the welded part, and was brittle. Shear rip was barely observable. A macroscopic observation of the ruptured face revealed that it was rough in general and the rupture occurred at random. In addition, defects including oxidation were observed. According to the SEM observation the rupture occurred generally in the dimple fracture surface, except for the defective area and the surface of the fracture surface in H<sub>2</sub> at room temperature. In addition, in some cases grain boundary fracture surface occurred in the vicinity of the surface of the rupture face in H<sub>2</sub> and at room temperature. As a result of cross section inspection, the cracks developed in the interior of the weld beads, and the starting points are generally produced in the interior of the beads. Regarding the influence of the hydrogen environment, the tensile strength, elongation, and contraction of area were lower than in He for all temperatures. However, there was a large amount of data scattering due to the presence of defects, so no conclusion was drawn from the result of this test alone.

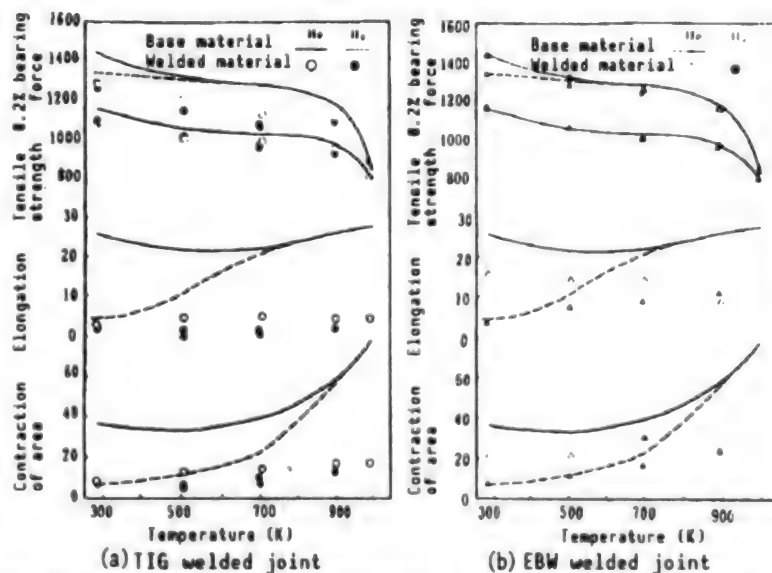


Figure 2. Tensile Characteristics of Welded Joint

Figure 2(b) shows the mechanical properties of the EBW welded joints for various temperatures in He and H<sub>2</sub> atmospheres. The EBW welded joints have the 0.2 percent bearing force and the tensile strength comparable to those of the base material, but their area elongation and contraction is lower than those of the base material. Fracture started in the base material in H<sub>2</sub> below 700 K,

and the welded areas in other circumstances. Shear rips were generally few, with rupture in approximately perpendicular direction to the axial direction. The width of the shear rip becomes large as temperature increases. The rupture face had fewer elevations and recesses than in the case of TIG, and there was only one starting point. The starting point was found on the surface of the base material part when in  $H_2$  of below 700 K, but was found in the weld bead in other cases. Cracks developed on the base material in  $H_2$  below 500 K, but developed in the interior of the bead in other cases. Rupture face was generally in the form of dimples except for the vicinity of the starting point in  $H_2$  below 700 K.

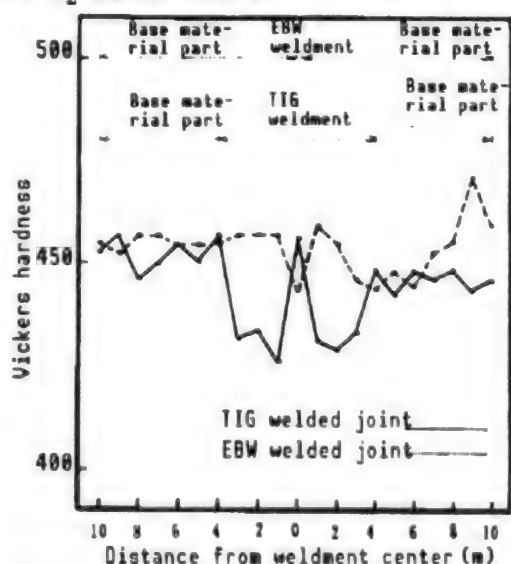
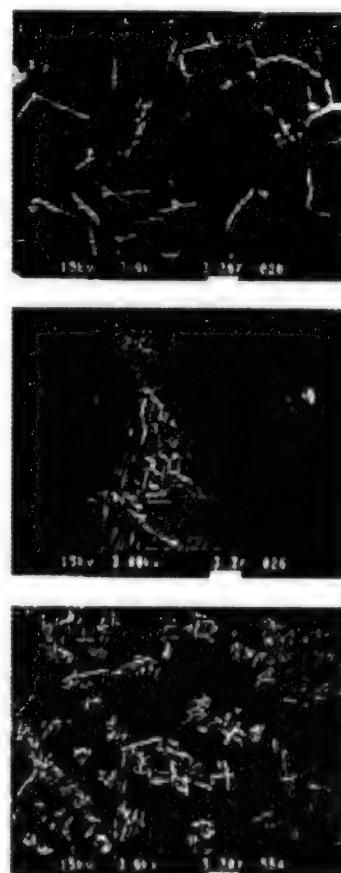


Figure 3. Hardness Distribution in Vicinity of Weldment

#### 4. Consideration

The welded joint is a kind of combined material since the weldment and the base material part are arranged in series. Accordingly, it is conceivable that there is generated a discontinuity of the tensile property in the weldment and the base material. In particular, in a TIG welded joint it is anticipated that the weldment is softened due to the degradation of the value of the 0.2 percent bearing force. Figure 3 shows the Vickers hardness distribution in the vicinity of the weldment. Although it is not pronounced for the EBW welded material, softening in the weldment is observable in the TIG welded material. It is said generally that the hardness is related to the proportionality limit, tensile strength, etc. Then, considering this fact combined with the result of the tensile test it is conceivable that in the TIG welded joint the proportionality limit is lowered in the weldment and the strain is concentrated in the weldment. Figure 4 shows the structural photographs of the base material, and TIG and EBW weldments. In contrast to the deposition of  $Ni_3Nb$  in the crystal grain boundary in the base material,  $Ni_3Nb$  is deposited in the form of



Top: mother material  
Middle: TIG; Bottom: EBW

Figure 4. Microstructure (x 3000)

dendrite in the TIG and EBW weldments. In contrast to the deposition of carbides distributed in the form of a relatively large aggregate in the base material, fine carbides are deposited surrounded by  $\text{Ni}_3\text{Nb}$  in the TIG and EBW weldments. The size of the carbide is the smallest in the EBW weldment. If one regards the portion surrounded by  $\text{Ni}_3\text{Nb}$  as a unit cell, the cell size of the weldment is nearly comparable to the grain size of the base material for the cell of EBW. In contrast, the size of the TIG cell is large. Generally, the resistance to deformation decreases with the increase in the grain size, so the size of the cell is believed to be specially related to the softening of the TIG weldment.

Figure 5 shows the true rupture strength of the base material, TIG, and EBW welded joints for the test in He. The number attached to the test point indicates the ratio of the slip rupture face to the area of the fracture face. It is said that the true rupture strength comes closer to the tensile separation force in the fractured area if the slip rupture face is smaller. From the figure it can be seen that the tensile separation force of the EBW weldment is smaller than that of the base material, and that of the TIG weldment is the lowest. This corresponds to the observation that the shear rip was found

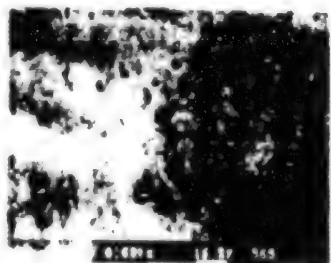
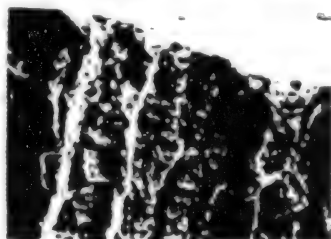


Figure 6. Photographs of Rapture Face and Cross Section (TIG welded joint)

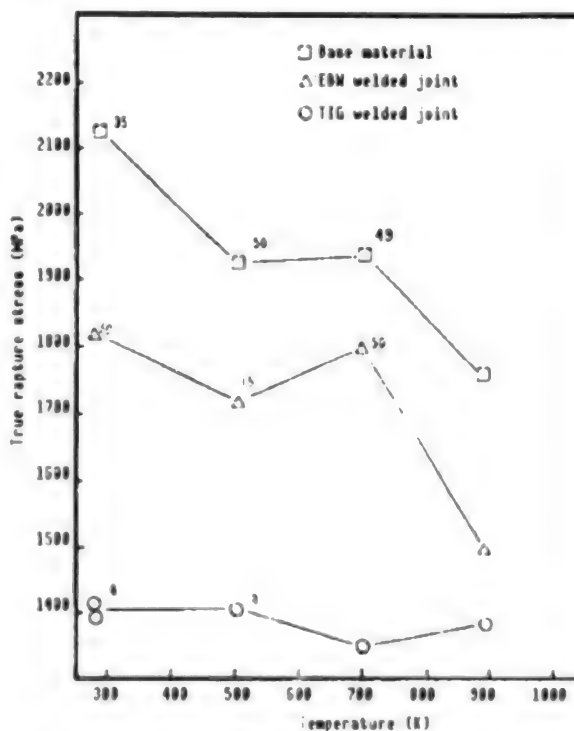


Figure 5. Comparison of True Rupture Strength

least in EBW welded joints, and it was seldom seen in TIG welded joints. In the TIG and EBW weldments, rupture proceeds in the weldment prior to the occurrence of slip separation due to reduction of the tensile separation strength. Figure 6 shows rupture face and a cross section of a TIG welding specimen. The rupture face reminds one of the dendritic structure of the weldment, and the matrix part shows fine dimple rupture face. From the conditions of the cross section, it is believed that cracks propagate along  $\text{Ni}_3\text{Nb}$ , and the rupture in the welded area of TIG seems to develop through the combination of propagation of the carbide rupture along  $\text{Ni}_3\text{Nb}$  and the dimple rupture in the matrix. Accordingly, it is conjectured that the separation strength depends upon the deposition form of  $\text{Ni}_3\text{Nb}$ , and it is the

smallest in the TIG weldment where TIG aggregates are large and are more continuous and it is smaller than that of the base material in the EBW weldment where the  $\text{Ni}_3\text{Nb}$  aggregates are dense, though they are discontinuous. Moreover, the influence of the hydrogen environment is considered to develop from the cracks in the surface. Since the size of the carbide in the EBW weldment is smaller than in the base material, the effect of cracks is less easily observed. Accordingly, for an EBW welded joint in  $\text{H}_2$ , rupture is considered to take place in the base material part.

## 5. Conclusion

For Inconel-718 welded joints, tensile tests in He and  $\text{H}_2$  environments were carried out to investigate the mechanical strength and the sensitivity to hydrogen embrittlement of the welded joints at normal and high temperatures. As a result, it is considered that the reduction in the mechanical strength of the welded joints shows itself as the softening of the weldment and the deterioration in the separation strength due to dendritic structure which is the structure of the weldment. In LE-7, the thermal strain often causes concern. Since the strain field of thermal strain is determined by the stress, it is believed that stress concentration due to softening of weldment tends to occur. In addition, due to reduction in ductility of the joint, the influence of an excessive strain is considered to be very dangerous because it tends to show itself in the form of immediate generation of cracks and fracture without revealing external deformation at all. A comparison of the EBW welded joint and the TIG welded joint shows that the tensile characteristic of the former is superior.

Furthermore, the EBW welded joint seems to have better hydrogen embrittlement property than the base material due to the deposition condition of the carbide.

## References

1. Jewett, R.P., Walter, R.J., Chandler, W.T., and Frohberg, R.P., "Hydrogen Environment Embrittlement of Materials," NASA CR-2163, 1973.
2. Lorenz, P.M., "Effect of Pressurized Hydrogen Upon Inconel-718 and Aluminum," NASA CR-100208, 1969.
3. Walter, R.J. and Chandler, W.T., "Influence of Gaseous Hydrogen on Metals," NASA CR-124410, 1973.
4. Araki, M., et al., "Research on Hydrogen Embrittlement of Rocket Materials," JOINT RESEARCH REPORT OF NASDA, MITI, 1988.
5. Yoshida, M., et al., "Trial Manufacture of Hydrogen Embrittlement Testing Device and Tensile Property of Turbine Materials in High-Pressure Hydrogen at High Temperature," NAL TR-1092, 1991.



## **Fracture Control of EFFU Graphite Epoxy Strut**

936C1015K Tokyo KOZO KYODO NI KANSURU KOENKAI in Japanese 15 Jul 92 pp 274-277

[Article by Michio Ito, NASDA, and Takane Watanabe, Tasuku Yamagata, and Tomoyuki Ikami, Ishikawajima-Harima Heavy Industries]

[Text] **Abstract:** The exposed facility flyer unit (EFFU) is installed on the space free-flyer unit (SFU) as a partial model of the space station JEM exposed facility. The SFU is scheduled to be launched by the H-II rocket in the winter of 1994, and returned to the ground by the space shuttle (STS) after six months in orbit. EFFU should be compared with safety requirements of STS, including fracture control requirements.

EFFU structure is mainly composed of graphite epoxy struts. The structural development model has completed all tests, and has been verified to satisfy structural requirements. The static load test for the prototype flight model (PFM) structure was completed in May 1992.

### **1. Introduction**

The exposed facility flyer unit (EFFU) is to be launched by the H-II rocket placed on the space free-flyer unit (SFU) and recovered by the space shuttle (NSTS). Because of this, it is necessary to consider the safety requirements, especially the fracture control requirement, of NSTS in addition to the conventional requirements on strength, rigidity, etc. The body structure of NSTS is a truss structure having struts made of a carbon fiber-reinforced plastic (CFRP) composite material, and the application of composites as struts to be put on-board NSTS is the first case in this country. Therefore, the suitability verification of the fracture control requirement of NASA was an important factor in its development. At present, manufacture and testing of the developed model have already been completed, and after examination of the detailed design in July of last year, a static load test of a prototype flight model (PFM) strut was completed in May of this year.

In this article, a brief summary of the fracture control of the composite strut, including the development result, will be presented.

## 2. Summary of Body Structure and Composite Struts

Figure 1 shows a sketch of EFFU in the state put on board SFU; Figure 2 shows the body structure of EFFU, and Figure 3 shows a sketch of composite struts.

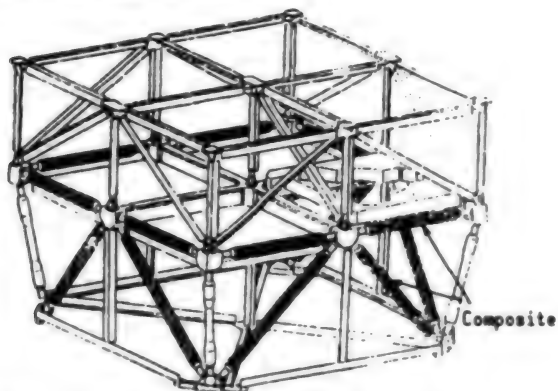


Figure 2. Sketch of EFFU Body Structure

## 3. NASA Requirements for Composites

The safety requirements of NSTS for structure are defined in NSTS1700.7B of which documents related to composites are found in NSTS14046 (structural requirements) and NHB8071.7B (fracture control requirements). Since the latter defines items that satisfy the former, the result from both parts is given in Table 1.

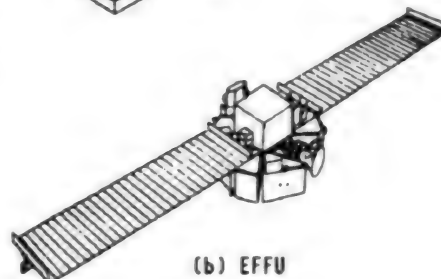
## 4. Suitability Verification Result to Fracture Control

In order to verify the suitability to the structural requirements including the fracture control requirements, experimental manufacturing test for elements, EM experimental manufacturing (structural development model) tests, and PF manufacturing tests were carried out.

In the element experimental manufacturing tests, along with the acquisition of various kinds of data, such as the strength of the composites (design tolerances), heat cycle load or evaluation of the influence of electron beam irradiation, the manufacturing process was established. The flow of the element experimental manufacturing tests is shown in Figure 4.

Following that, in the structure development model tests, a static load test, sine wave vibration test, acoustic test, impact test, etc., were carried out as the body structure assembly level tests, and confirmed that the requirements for structural strength are satisfied. The flow of the development model tests is shown in Figure 5. For composite struts, a proof test and product

(a) Configuration on-board SFU



(b) EFFU

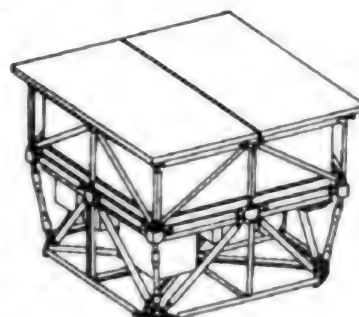


Figure 1. Situation Put On-Board SFU



Figure 3. Composite Strut

Table 1. Verification Result of EFFU Composite Compared to NASA Requirements  
 ●: Already demonstrated

Requirement	Verification result/plan	Verification status		
		Element trial manufacture	EM	PFM
1. For composite/bonded structures, only reliable manufacturing processes and control (coupon test, sampling techniques, etc.) that match established aerospace industry practice, should be employed  Test specimen should be designed and manufactured according to same requirements, drawings, and specifications as the flight product	1) Manufacture was carried out under quality assurance control of makers (IHI) adapted to NASDA requirements  2) No basic changes of materials (specifications), fabrication drawing, and manufacturing processes in element trial manufacture, EM, and PFM (see Figure 7)	●	●  ●	●  ●
2. Data to be referenced should be tolerances of material data: MIL-HDBK-17 or minimum assured values of makers or values based on statistical data for specific manufacturing process (requires approval of NSTS structure WG)	1) Applied tolerances corresponding to B value from data obtained by element trial manufacture test  2) Influence of resistance to environment such as heat cycle and electron beam irradiation was confirmed by tests (see Figure 4)	●  ●		
3. Fracture critical composite/bonded structure should satisfy either: a) apply proof test for more than 120% of limited load, b) damage allowance test	1) For whole flight components, load of over 120% of limited load was applied under temperature condition in which load is applied (standardization was load at STS landing and temperature)  2) Ultrasonic flaw detection test given before and after proof test (see Figures 6, 7, and 9)	● Normal temperature  ●	● Normal temperature  ●	● High temperature  ●
4. Protection of fracture critical composite/bonded structures (flight components) from impact at time of handling and final assembly	1) Individual items protected by container, and assembled items protected by air cap (see Figure 8)		●	●

Note: High temperature condition at STS landing.

protection were carried out similar to PFM. For PFM body structures, a proof test exceeding 120 percent of the limiting load was carried out for all products on the composite strut level. Then, static load tests were carried out on the body structure assembly level to perform confirmation of the products as structures, and verification of the structure development model concerning the composites.

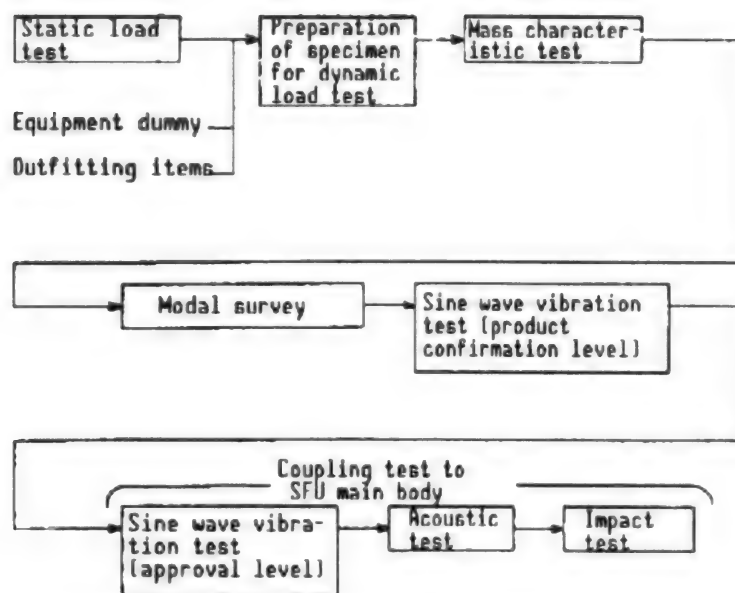


Figure 4. Flow of Trial Manufacture Tests

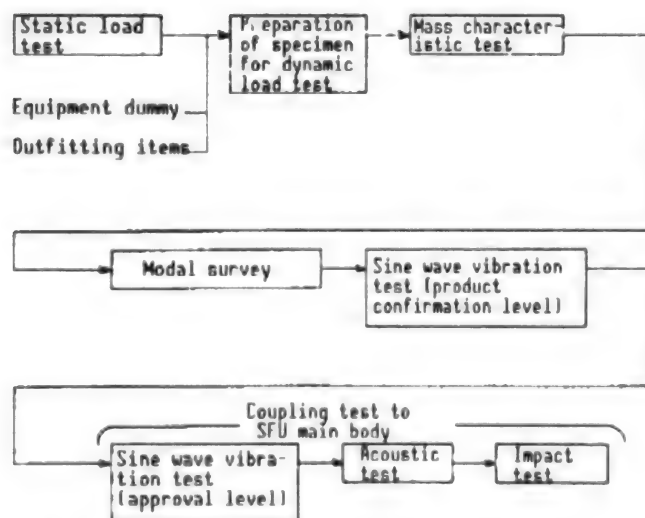


Figure 5. Flow of Structure Development Model Tests

In addition, prior to the PFM manufacture, strength tests for evaluation of the influence of the ambient temperature were carried out for the testpieces on the strut level. As a result, strength to the thermal stress (including the local stress in the adhesion part) for the load conditions and the ambient temperature at the time of NSTS landing which becomes critical in the design, was confirmed. A summary of the result is shown in Figure 6.

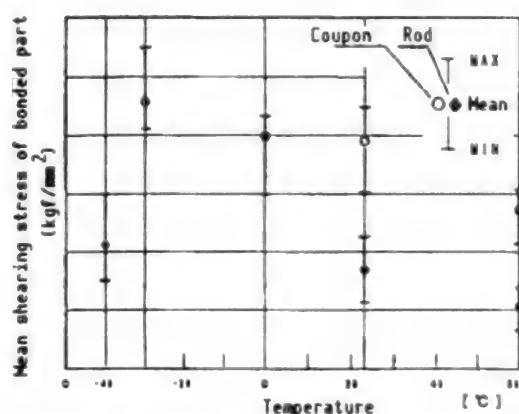


Figure 6. Ambient Temperature and Strength of Composites

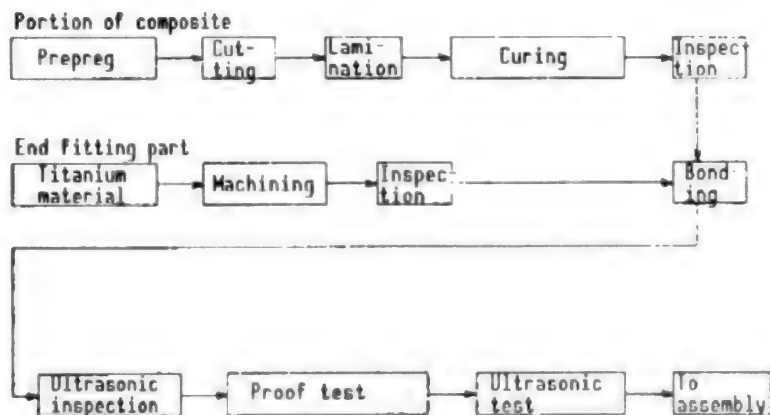


Figure 7. Manufacture Flow of Composite Strut

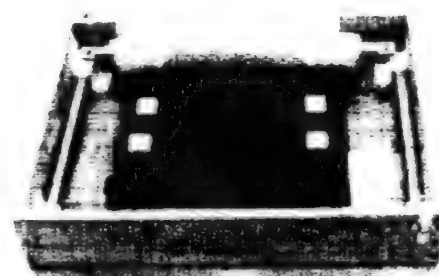


Figure 8. Protection of Composite

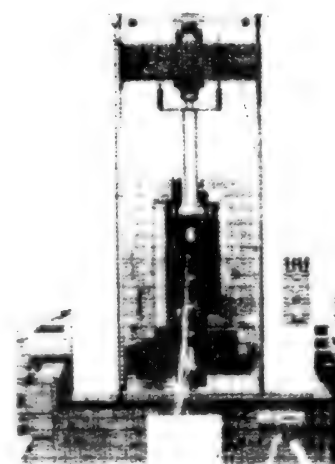


Figure 9. Proof Test Configuration

The verification result for the fracture control requirements for the CFRP rods of the EFFU body structures obtained by the above tests is shown in Table 1.

## 5. Conclusion

The fracture control plan for CFRP rods of the EFFU body structure described above was approved by NASA Safety Investigation, Phase II, in September of last year, and the validity of our approach was confirmed. In this way the guidelines were established in applying composites to spaceplane systems using STS in the future. The EFFU airframe therefore poses no problems as an airplane product now that PFM has been produced and the static load tests have been completed.

## **Experiment of CFRP Pressurized Composite Tank for Artificial Satellites**

936C1015L Tokyo KOZO KYODO NI KANSURU KOENKAI in Japanese 15 Jul 92 pp 310-313

[Article by Kouichi Miyoshi, Iton Cho, Kenichi Kimoto, and Mitsunori Nakamura, Ishikawajima-Harima Heavy Industries]

[Text] **Abstract:** This report describes the test result of a pressurized composite tank which is under development for aerospace use. A titanium alloy carbon fiber reinforced tank burst at the pressure of 580 kg/cm<sup>2</sup>G in a test. Calculated burst pressure by the finite element method (FEM) agreed with actual burst pressure approximately.

### **1. Introduction**

In recent years, application of carbon fiber-reinforced plastics (CFRPs) in the aerospace industry has been remarkable. Even for rockets and artificial satellites CFRPs are being used frequently to reduce the weight. In the past, the pressure vessel used for the propulsion system of artificial satellites, etc., was made of metal, but lately a composite pressure vessel whose surface is reinforced with aramid fiber to reduce the weight is beginning to be used. In this research, we experimentally manufactured a CFRP pressure vessel (referred to hereafter as "tank") in which a thin metallic liner is reinforced with carbon fiber which has specific strength superior to aramid fiber, and is expected to yield further weight reduction, and carried out fracture tests. Further, structural analysis by the finite element method (FEM) was done to estimate the fracture pressure, and the result was compared with experimental results and discussed.

### **2. Experimental Manufacture of Tank**

#### **2.1 Principal Items of Tank**

The principal items of the pressurized tank experimentally manufactured this time are shown in Table 1. Further, Figure 1 shows a schematic shape of a metallic liner prior to filament winding formation (FW). It is a polar mount type spherical composite tank with an outer diameter of 304.6 mm, having an inlet and an outlet port on its diametrical extremities.



Table 1. Principal Items of CFRP Pressure Tank

		Description
Outer diameter $D_0$		$\phi$ 304.6 mm
Capacity V		14.6 [1]
Liner part	Material	Ti-6Al-4V (annealed)
	Sheet	General part 0.6 mm Weldment 1.0 mm
Fiber-reinforced part	Material	CFRP (T-800H/BMI)
	Number of layers	12 layers
	Thickness	5.65 mm (Volume average)
Weight W	Liner part	1.445 kg
	Fiber-reinforced part	2.665 kg
	Total	4.11 kg
Content of fiber volume		61 %

Three kinds of metals for the liner, SUS system, Al alloy, and V, were examined, and we selected Ti-6Al-4V (annealed) for its magnitude of specific strength, magnitude of fracture toughness, and excellent weldability. For the fiber, we used carbon fiber with a high specific strength and specific modulus of elasticity (TORAYCA T-800H), and a bismaleimide (BMI) resin was used as the matrix resin to be used for the CFRP part.

The fiber volume content of the CFRP part measured after experimental manufacture was about 61 percent. The weight of the tank was about 4.1 kg.

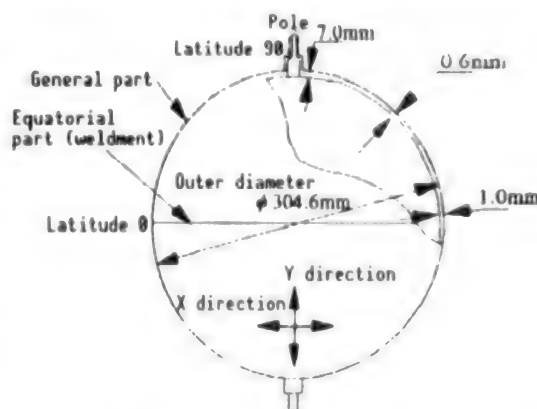


Figure 1. Shape of Metallic Liner

## 2.2 FW Formation

A conceptual diagram of the FW formation of the tank is shown in Figure 2. The FW formation for the experimental manufacture of the tank was executed so as to have 12 layers of CFRP on top of the liner part. In determining the FW formation parameter, pattern design was carried out so as to have fracture initiated from the general area (vicinity of the equator) of the tank.

A photograph of the tank after FW formation is shown in Figure 3.

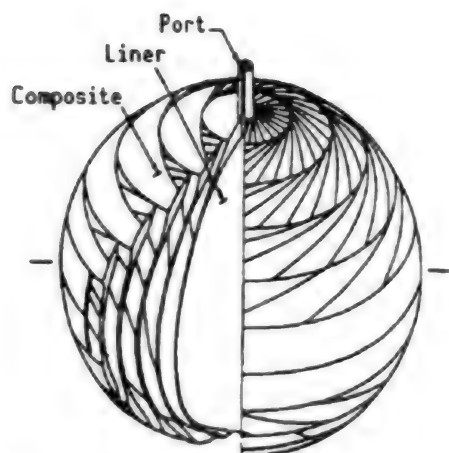


Figure 2. Conceptual View  
for FW Formation



Figure 3. Tank After FW  
Formation

### 3. Estimation of Pressure at Tank Fracture by Structural Analysis

#### 3.1 Fiber Orientation Angle and Thickness of CFRP Part

In performing structural analysis by the finite element method, it is necessary to estimate the direction and thickness of the fiber. In this work, a theoretical expression was derived in terms of a three-dimensional spherical model to estimate the fiber orientation angle and the thickness of the CFRP part.

#### 3.2 Model and Method of Analysis

An analytical model was prepared based on the lamination information and the shape of the metallic liner of the CFRP part described in the foregoing. It is shown in Figure 4. The liner was modeled using 84 two-dimensional four-node shell elements, and the CFRP part was modeled using 80 two-dimensional four-node composite elements. The boundary conditions were set so as to be a part of the sphere. In the finite element analysis, plasticity was taken into account for the liner whereas elasticity alone was taken into account for the CFRP part. Non-linear analysis was performed for materials in general. However, analysis was done by assuming, for the CFRP part, small values from the beginning for the elastic modulus  $E_T$  in the perpendicular direction to the fiber and the modulus of shearing elasticity  $G_{LT}$ , by allowing for the generation of cracks along the fiber direction even for the low state of the inner pressure of the tank. In the estimation of the fracture pressure it was evaluated based only on the maximum stress ( $\text{Max } \sigma_L$ ) generated in the fiber direction of the CFRP part. In other words,  $\text{Max } \sigma_L$  was extracted for each

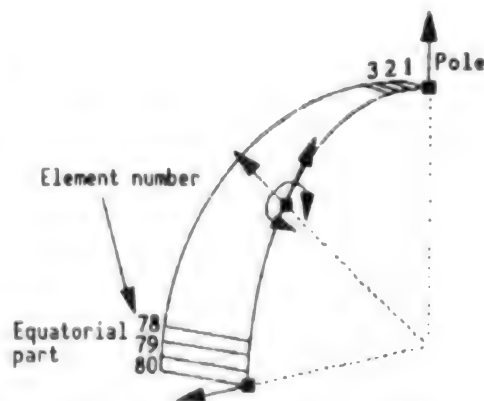


Figure 4. Analytical Model

modeled element, and the pressure at which this value exceeds the strength ( $\sigma_b$ ) in the CFRP fiber direction was regarded as the tank fracture pressure. The value of  $\sigma_b$  was obtained by NOL ring test, and it was taken to be 280 kg/mm<sup>2</sup> in this work.

### 3.3 Result of Analysis

The stress distribution in which Max  $\sigma_L$  is extracted for each element is shown in Figure 5. From the figure it can be seen that fracture occurs in the general part near the equatorial zone at the tank internal pressure P of about 400 kg/cm<sup>2</sup>.

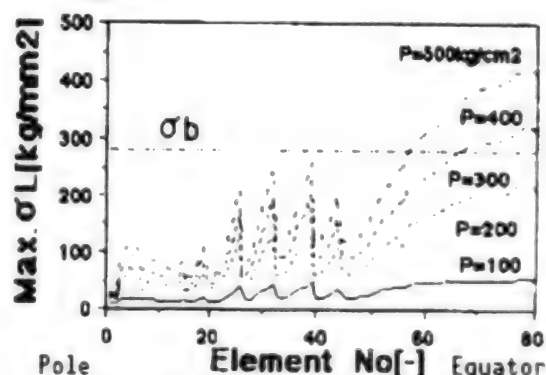


Figure 5. Maximum Stress Distribution in Fiber Direction

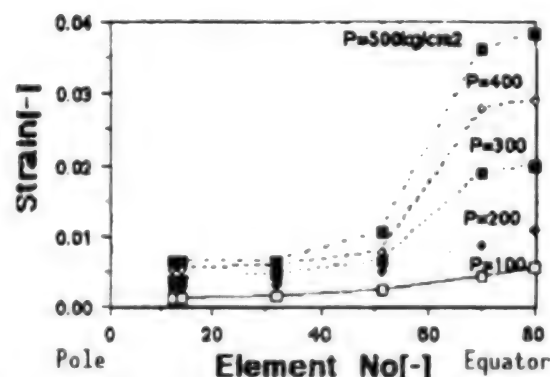


Figure 6. Strain Distribution in Liner (X direction)

The strain distribution of the liner are shown in Figures 6 and 7. From these figures it can be seen that in the X direction strain increases as it approaches the equatorial zone, whereas in the Y direction strain is large in the area near the port.

## 4. Tank Fracture Test

### 4.1 Outline of the Test

The fracture test of the tank was performed using a pressure testing machine with maximum pressurizing capability of 1,500 kg/cm<sup>2</sup>. The tank was put in a perfectly free state, pressurized with ion-free water, and the strain was measured on the surface of the metallic liner and the surface of the CFRP part (for the X and Y directions on the liner surface, and in the fiber direction on the CFRP part) using strain gauge.

### 4.2 Result of Fracture Test

A summary of the test is shown in Table 2. When the performance factor (PF) which represents the performance of the tank was evaluated for reference using fracture pressure  $P_b = 580$  kg/cm<sup>2</sup>, we obtained

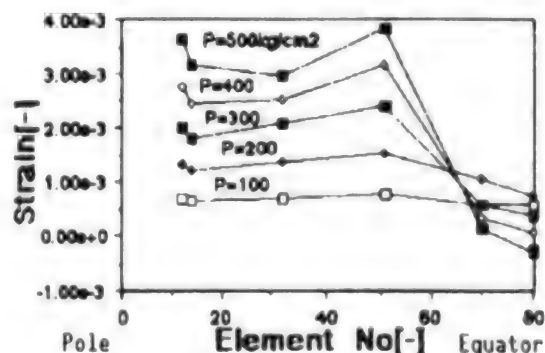


Figure 7. Strain Distribution in Liner (Y direction)

$$PF = P_b \cdot V/W = 2.060 \cdot 10^7 \text{ mm}$$

In this case a weight reduction of 34 percent compared with a tank made exclusively of Ti (STR material) was achieved.

**Table 2.** Summary of Fracture Test Result

Item	Description
Fracture pressure	Approximately 580 kg/cm <sup>2</sup>
Maximum liner strain (X direction)	$\epsilon_x = 2.21 \%$ (Latitude 0)
Maximum liner strain (Y direction)	$\epsilon_y = 2.88 \%$ (Latitude 51)
Maximum strain on CFRP part (fiber direction)	$\epsilon = 1.7 \%$ (Latitude 20)

The result of strain measurement using a strain gauge installed aligned with the fiber direction on the surface of the CFRP part is shown in Figure 8. In addition, the results of the strain measurement taken by strain gauges installed on the surface of the metallic liner are shown in Figures 9 and 10.

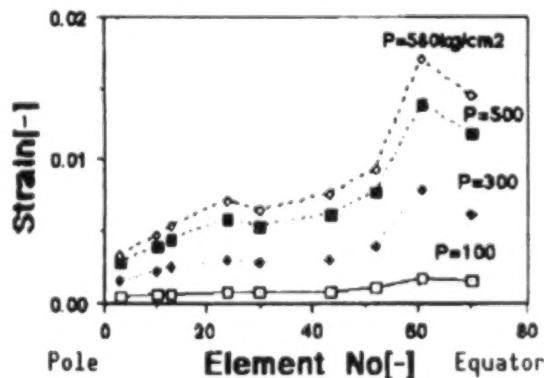


**Figure 8.** Strain Distribution (in surface fiber direction)

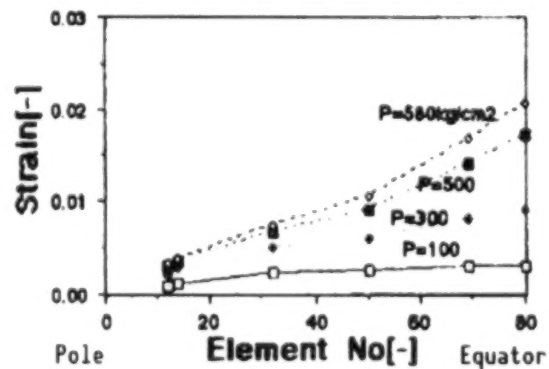


**Figure 9.** Strain Distribution Liner Surface (X direction)

It can be seen that the strain distribution in the fiber direction on the surface of the CFRP part and the maximum strain distribution in the fiber direction by analysis show good qualitative agreement. Further, for the strain on the surface of the metallic liner, the qualitative tendency agrees relatively well with the analytical result, but quantitatively there still remains a large disagreement.

## 5. Consideration

The analysis was revised because the actual fracture occurred at a pressure which was higher over 100 kg/cm<sup>2</sup> than the analytically estimated value. The changes in the analysis are the following two points.

(1) The sheet thickness (0.6 mm) of the welded part of the metallic liner used in the calculation, which had been taken to be the same as that of the general part, was changed to the same value as the actual model (1.0 mm).

(2) In the thermal setting treatment given after the FW formation, the influence of the residual stress in this formation setting was taken into account.

The result of the recalculation after the above changes is shown in Figure 11. This figure shows the stress distribution of  $\text{Max } \sigma_1$ . From the figure it can be seen that the generated stress at some places exceeds  $\sigma_b$  when the pressure inside the tank becomes 500 kg/cm<sup>2</sup>. This can be said to be in relatively good agreement with the test result. However, it cannot necessarily be said that the strain is in good agreement, and requires further detailed investigation. We plan to continue to examine the fracture process of the tank.

## 6. Conclusion

In this research, experimental manufacture of the CFRP pressure vessel, fracture test estimation of fracture pressure in the structural analysis by finite element method, and comparison with the experimental result, was accomplished. Future tasks include:

- (1) To correlate results of tests including that of stress to the analytical result.
- (2) To develop an optimum program for the FW formation pattern in order to realize further weight reduction.

- END -

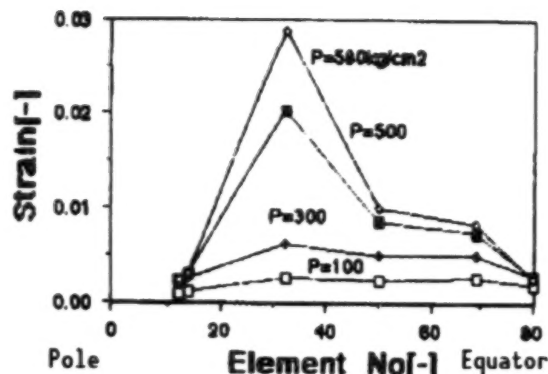


Figure 10. Strain Distribution on Liner Surface (Y direction)

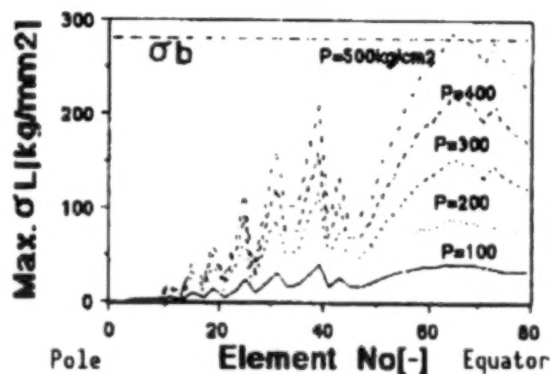


Figure 11. Maximum Stress Distribution in Fiber Direction (Analytical result)

**END OF**

**FICHE**

**DATE FILMED**

23 APRIL 1993



